Mainstreaming Commercial CSP Systems: A Technology Review

Angel G. Fernández,[a,c*] Judith Gomez-Vidal,[b] Eduard Oró,[c] Alan Kruizenga,[d] Aran Solé,[e] Luisa F. Cabeza[c]

[a] *Energy Development Center, University of Antofagasta, Av. Universidad de Antofagasta 02800, Antofagasta, Chile*

[b] *National Renewable Energy Laboratory, 15013 Denver West Parkway, 80401, Golden, CO, USA*

[c] *GREiA Research Group, INSPIRES Research Centre, Universitat de Lleida, Pere de Cabrera s/n, 25001 Lleida, Spain*

[d] *Kairos Power, 580 2nd Street, Oakland, CA, 94607, USA*

[e] *Department of Mechanical Engineering and Construction, Universitat Jaume I, Campus del Riu Sec s/n, 12071 Castelló de la Plana, Spain*

**Corresponding author: angel.fernandez@diei.udl.cat*

Abstract

In this review, we summarise the current status and new trends in concentrating solar power (CSP) technology, analysing the technology cost and their evolution during the last years, with special focus on thermal storage. Moreover, we have carried out a comprehensive review of the molten salts used and proposed in CSP commercial plants. Nitrates, nitrites, chlorides, and carbonates are presented, including their corrosion aspects with common alloys as well as the different possibilities available in the literature to replace them (ternary and quaternary nitrate molten salt) or improve them (addition of nanoparticles). Finally, we have proposed the key factors for a successful new generation of CSP plants, with special focus on high-temperature molten salts (carbonates and chloride blends) and the main important materials requirements for CSP system components.

Keywords: Concentrating solar power; Thermal energy storage; Molten salts

1. Introduction

1.1. Commercial CSP plants. Current technology and dispatchability

In recent decades, the study of renewable energy and its practical applications has greatly expanded. Solar energy is one of the technologies that has benefited most from international commitments geared toward reducing and controlling the emissions of CO_2 from energy storage systems.

The real birth of concentrating solar power (CSP) as an industry came in California in the 1980s with the construction of nine separate parabolic-trough-based 'Solar Electric Generating Systems' (SEGS), with 354 megawatts-electric (MWe) of installed capacity.

In 1982, the U.S. Department of Energy, along with an industry consortium, began to operate Solar One, a 10-MW central-receiver demonstration project. This project established the feasibility of power tower systems using a heat-transfer fluid to produce steam, which powered a conventional turbine to produce electricity. In 1996, Solar Two demonstrated how solar energy can be stored efficiently and economically to produce electricity even when the sun is not shining.

CSP plants concentrate sunlight, which is converted to high-temperature thermal energy for direct or indirect operation of a heat engine and electricity generator. The plants generate electricity with a thermal power cycle similar to that used in conventional fuel-fired power plants. Due to recent developments, China, India, and South Africa are leading the rankings of installed CSP capacity. In 2016, 110 MWe of CSP capacity came online, bringing global capacity to more than 4,800 MWe by year end. This was the lowest annual increase in total global capacity in 10 years—at just over 2%—but activity suggests a rebound in 2017 by as much as 900 MWe following REN21 predictions [1]. Moreover, taking into account the list of projects currently being constructed and being developed (projects with a signed agreement, but actual construction still pending), another 8,543 megawatt-hours-electric (MWhe) will be added in the next several years [2,3]. CSP continued its advance into developing countries that have high direct normal irradiance (DNI) and specific strategic and/or economic alignment with the benefits of CSP technology. In this respect, CSP is receiving increased policy support in countries with limited oil and gas reserves, constrained power networks, a need for energy storage, or strong industrialisation and job creation.

Four generally accepted CSP technologies are characterized by concentrating sunlight by reflection onto a receiver, as illustrated conceptually in

Figure **1**. Linear Fresnel reflectors (LFRs) and parabolic trough collectors (PTCs) are line-focus solutions that concentrate sunlight on a linear receiver, which typically is a steel tube with an evacuated glass cover for insulation. These technologies have fundamental limits that are particularly related to the theoretical concentration ratio [4,5]. In contrast, central receiver and parabolic dish systems are point-focus solutions that can achieve far higher concentration ratios but require proportionally more effort in tracking accuracy.

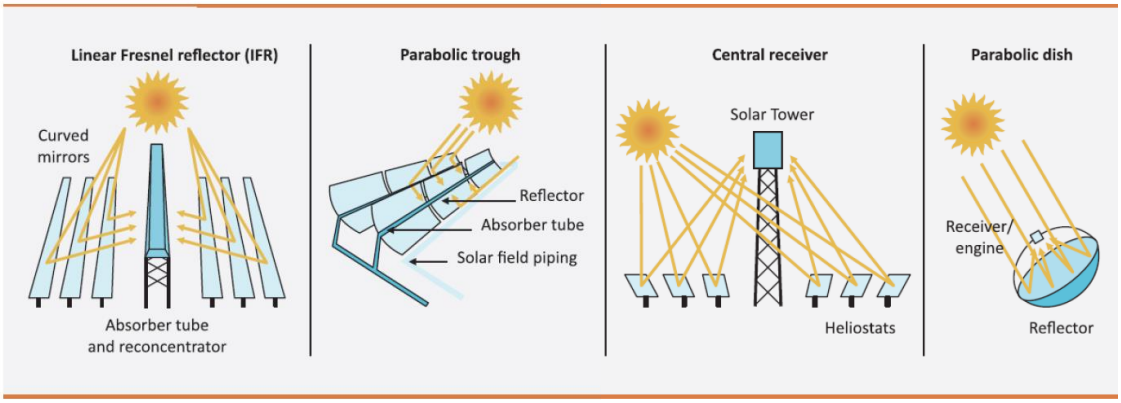

Figure 1. Generally accepted CSP technology types [4].

In 2013 [6], plants based on PTCs were the most commercially attractive and widely installed CSP technology, which use synthetic or organic oil as the heat-transfer fluid (HTF). But today, both PTC and central tower technologies dominate the market. LFR and parabolic dish technologies are still largely overshadowed, apart from some smaller plants in the development and construction phases. Figure 2 presents the CSP worldwide power capacity under construction and development, shown as a function of technology type. More PTC plants (30 plants) are being built and designed, but the total power capacity under construction and development for power tower plants (5,383 MWhe) is

twice that of the power capacity of PTs (2,681 MWhe). It is also interesting that the average power capacity for PTC and power tower plants is 89 and 207 MWhe, respectively. Note that although there are some LFR and parabolic dish projects worldwide, their commercialization is still far behind the other technologies.

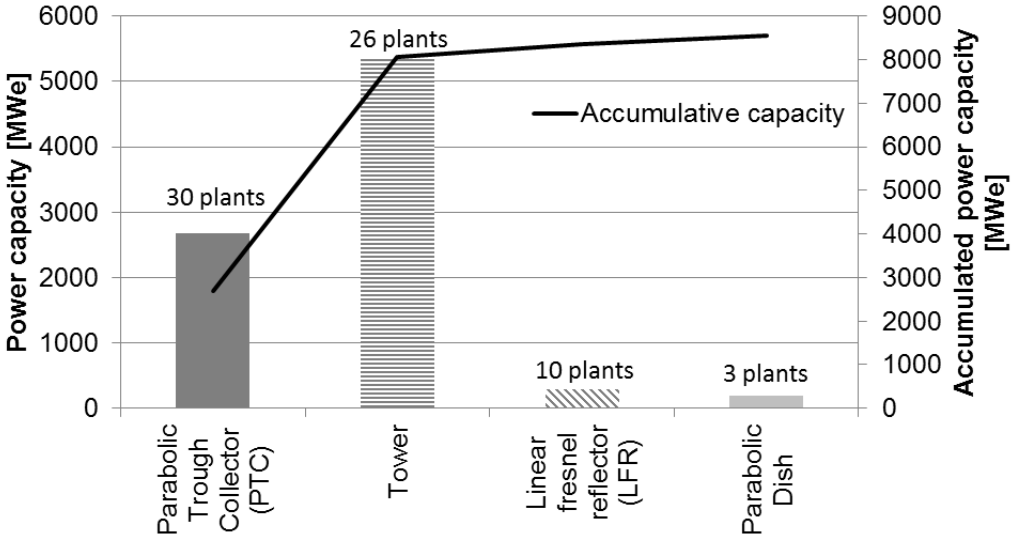

Figure 2. CSP worldwide power capacity under construction/development as a function of the technology [6].

CSP is unique among renewable energy generation sources because it can easily be coupled with thermal energy storage (TES) as well as conventional fuels, making it highly dispatchable. Most new CSP plants are being developed with TES, which continues to be viewed as central to the competitiveness of CSP by providing the flexibility of dispatchability. In 2016, the total CSP TES global capacity was about 11,900 MWh_{th} [1]. Molten-salt technologies are the dominant commercial solution deployed today and they account for 75% of the globally deployed TES used for electricity applications [7].

TES technologies operate with the goal of storing energy for later use as heating or cooling capacity, and they could be an important tool in achieving a low-carbon future. These technologies decouple energy supply and demand, providing a valuable resource to system operators. The benefits yielded by TES systems are as follows: (a) a cutback in real-time net power variability in the event of pool solar radiation, (b) an extension of the whole production period, and (c) a possible rearrangement of production toward high-

price periods, resulting in an increase of the CSP power dispatchability. An energy storage system can be described in terms of the following key performance indicators [8]:

- Capacity [MWh]: defines the energy stored in the system and depends on the storage process, medium, and size of the system.
- Power [MW]: defines how fast the energy stored in the system can be charged and discharged.
- Efficiency [%]: the ratio of the energy delivered during discharge to the energy needed to charge the storage system. It accounts for the energy loss during the storage period and the charging/discharging cycle.
- Charge and discharge times [h]: define how much time is needed to charge or discharge the system.
- Cost [€/kW or €/kWh]: refers to either capacity (€/kWh) or power (€/kW) of the storage system. It can be referred to as thermal or electric cost, and it commonly includes the storage material itself, the heat exchanger for charging and discharging the system, and the cost of the space and/or enclosure for the TES.

A basic first-order assessment can be performed calculating the capacity factor (C_f) of the CSP plant as shown by Eq. 1:

$$C_f = \frac{E_{plant}}{P_{net} \cdot 8760}\ , \qquad \text{Eq. 1}$$

where E_{plant} is the expected annual electricity produced (as defined by Eq. 2) in MWhe, and P_{net} is the net output power in MWe.

$$E_{plant} = I_b \cdot A_{ref} \cdot \eta_{plant}\ , \qquad \text{Eq. 2}$$

where I_b is the long-term average annual DNI in MWhth/m^2, A_{ref} is the concentrator aperture area of the plant, and η_{plant} is the total annual plant efficiency:

$$\eta_{plant} = \eta_{optical} \cdot \eta_{receiver} \cdot \eta_{power}, \qquad \text{Eq. 3}$$

where $\eta_{optical}$, $\eta_{receiver}$, and η_{power} are, respectively, the process efficiencies for collecting and concentrating sunlight, its conversion to thermal energy, and its net conversion of power production, which incorporates the efficiency of TES.

For some of the CSP plants being constructed and developed, the expected annual electricity produced is known; therefore, the capacity factor can be calculated. Figure 3 shows the capacity factor for tower technology and Figure 4 shows the capacity factor for PTC and LFR CSP plants. On one hand, for tower technology, there is a clear trend: as plant capacity power increases, capacity factor increases. A capacity factor higher than 50% represents a CSP plant with a significant amount of storage. On the other hand, for PTC and LFR, where some of the plants do not include TES, there is no trend. Note that for these technologies, the CSP plant capacity is lower than in the tower case; therefore, a lower capacity factor is also present.

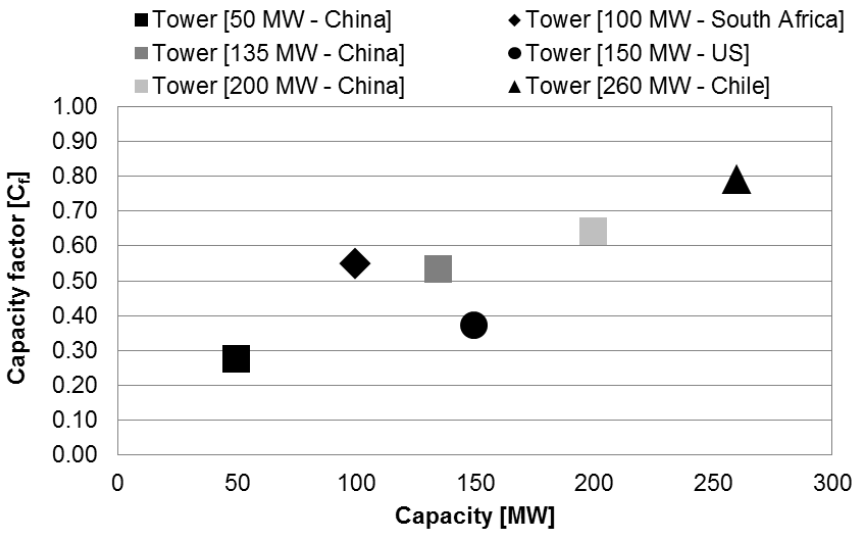

Figure 3. Capacity factor for tower technology CSP plants under construction and development.

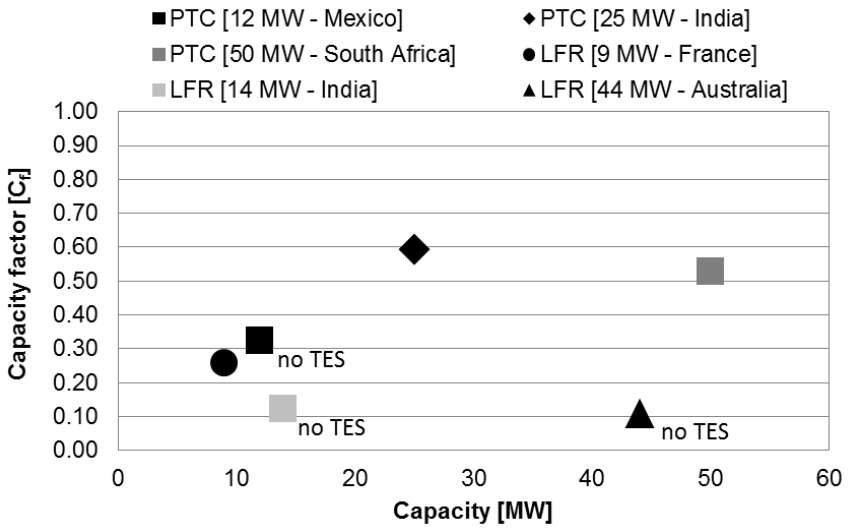

Figure 4. Capacity factor for PTC and LFR technology CSP plants under construction and development.

As stated previously, TES systems serve a key role in the dispatchability of CSP plants, and Figure 5 shows the capacity factor for different CSP technologies as a function of storage capacity in hours. The clear trend within the commercial CSP plants analysed is that the higher the storage capacity, the higher the capacity factor.

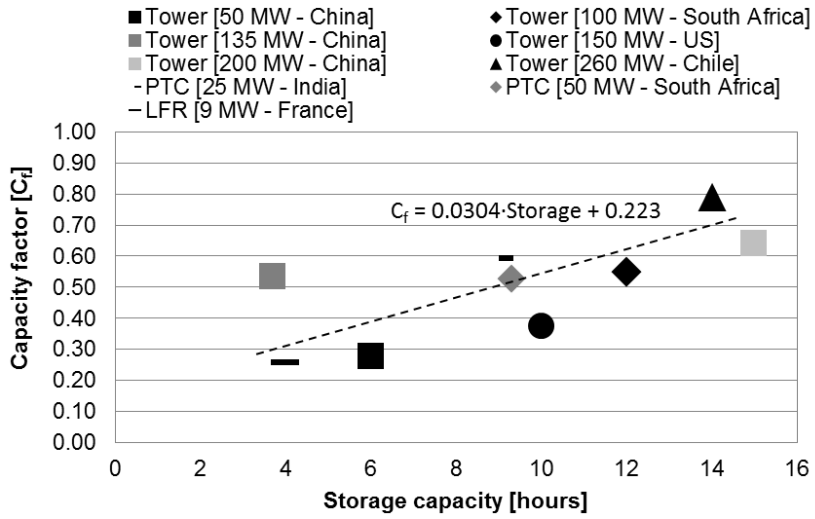

Figure 5. Capacity factor for PTC and LFR CSP plants under construction and development.

1.2. TES configuration proposed for CSP plants

TES solutions for CSP plants can be classified as active or passive systems [4]. When the storage medium is a fluid and can flow between the storage tanks, the system is referred to as an active type. If the storage medium is also used as the HTF, the system is referred to as direct-active. An additional heat exchanger is needed when the storage medium and HTF are different, and the unit is referred to as an indirect-active type. When the storage medium is solid, the HTF passes through the storage material only for charging and discharging. Such a system is referred to as a passive type. Figure 6 shows various examples of TES configurations classified as active and passive storage systems.

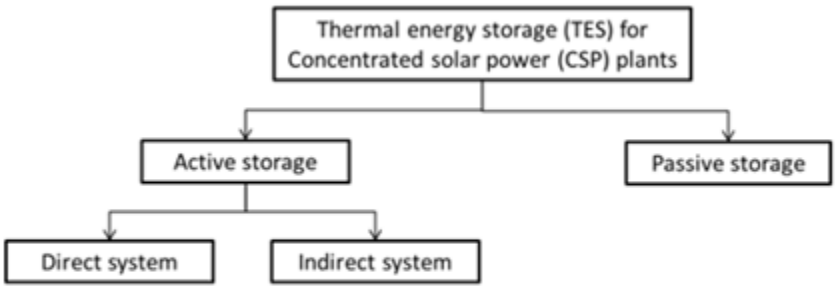

Figure 6. Categorization of TES systems for CSP plants [4].

The molten-salt two-tank direct system consists of storage where the HTF—the molten salt—is stored directly in a hot tank to be used during cloudy periods or nights. The cooled HTF is pumped to the other (cold) tank prior to being pumped and heated again. This configuration eliminates the need for costly heat exchangers. Figure 7 schematically shows the process flow for a typical solar power plant with an active direct molten-salt TES system. Steam accumulators are pressurized vessels that can provide storage by accumulating excess steam produced by the receiver for later release to drive the turbine. Figure 8 schematically shows the process flow for a steam tower plant with an active direct-steam-accumulation TES system.

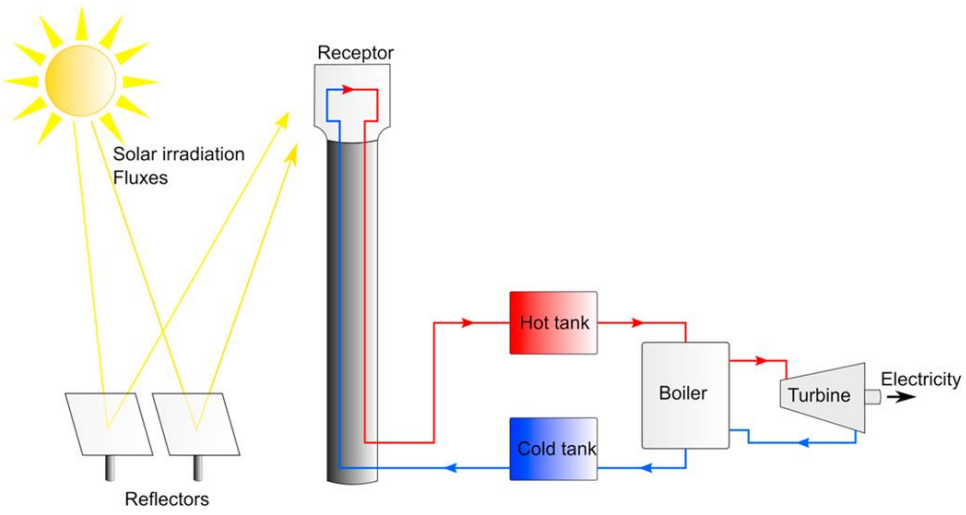

Figure 7. Molten-salt two-tank direct concept for TES integration in CSP plants [9].

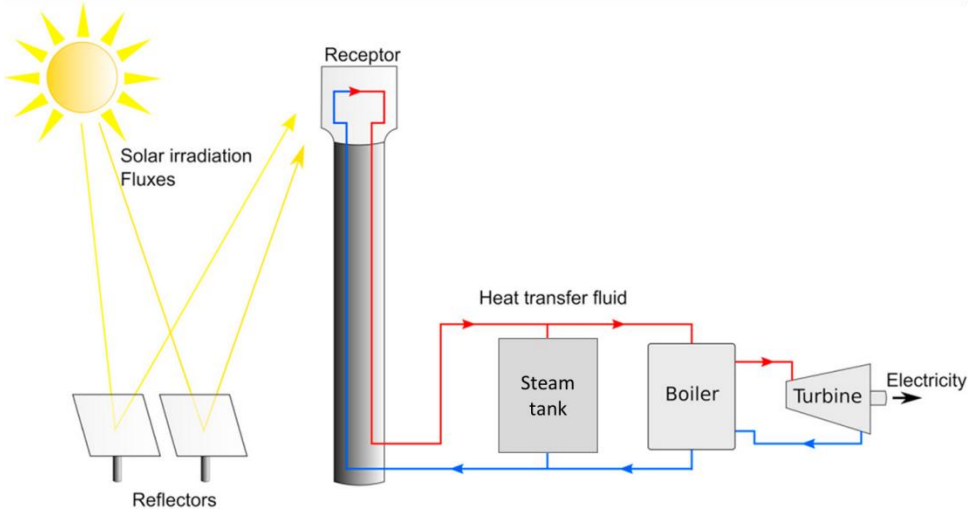

Figure 8. Steam-accumulator concept for TES integration in CSP plants [9].

As described before, in an active indirect system, a second medium is used for storing the thermal energy; therefore, a heat exchanger is needed to transfer the energy from the HTF that circulates in the solar field to the storage medium. To date, the molten-salt two-tank indirect system with synthetic oil HTF is the most common implementation for parabolic troughs. Figure 9 schematically shows the process flow for a typical solar power plant with an active indirect molten-salt TES system.

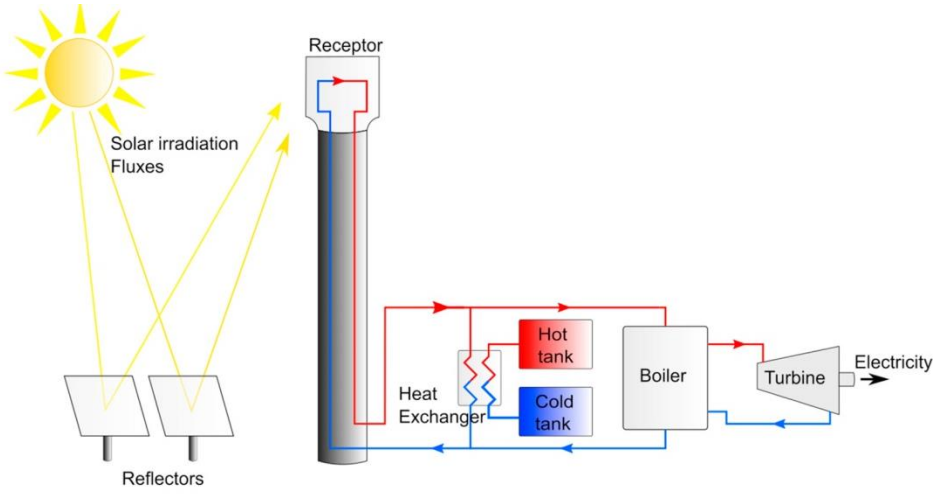

Figure 9. Molten-salt two-tank indirect concept for TES integration in CSP plants [9].

Finally, Figure 10 schematically shows the integration of a concrete storage concept that is categorized as passive storage in CSP plants.

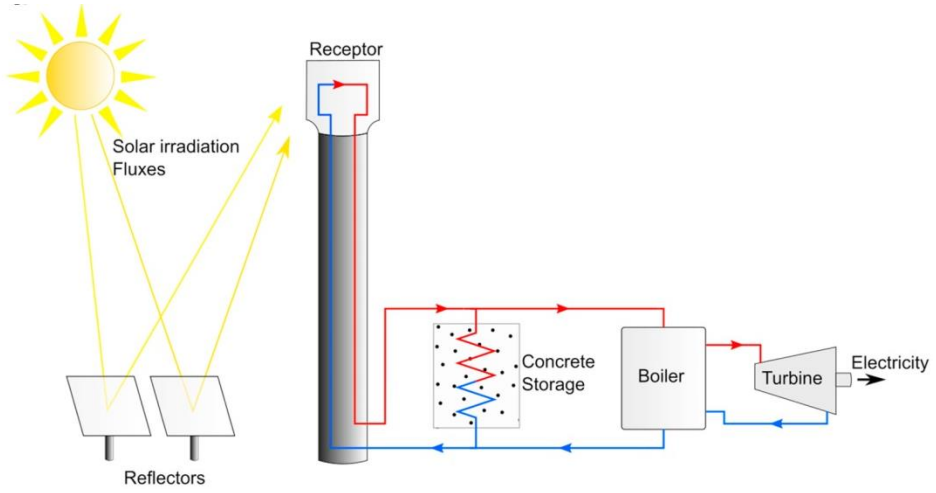

Figure 10. Concrete storage concept for TES integration in CSP plants [9].

To date, in active storage systems, molten salt as direct and indirect storage is the most widespread storage material in CSP commercial applications due to its good thermal properties and reasonable cost. However, some commercial CSP plants have steam accumulators and concrete storage tanks as TES solutions. Currently, of the 69 CSP plants under construction or development, 50 have TES systems [2,3]. Figure 11 shows the number of CSP plants as a function of the TES categorization described above. Note that more than 80% of the TES systems are based on molten-salt solutions.

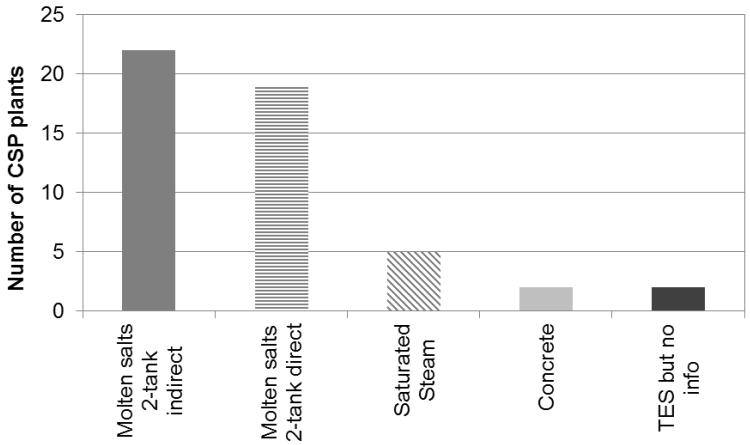

Figure 11. Number of CSP plants under construction/development as a function of the TES categorization.

1.3. Cost analysis of commercial CSP plants

Following the latest solar thermal electricity roadmap from the International Energy Agency (IEA) [10], as technologies mature, the cost of CSP plants is expected to be halved by 2030 (compared to 2015). The capital expenditure (CAPEX) is assumed to follow a 10% learning rate (i.e., diminish by 10% for each doubling of cumulative capacities). Figure 12 shows the CSP investment cost projections from 2015 to 2050 in the hi-Ren Scenario, which envisions CSP electricity production up to 11% of global electricity by 2050 (renewables provide 79%), from the IEA report.

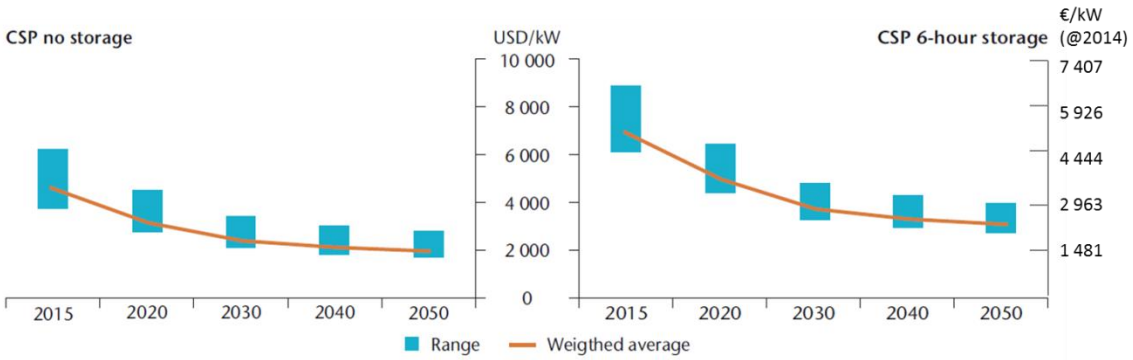

Figure 12. CSP investment cost projections in the hi-Ren Scenario [10].

Aligned with this, Figure 13 and Figure 14 show the CAPEX for commercial PTC and tower CSP plants, respectively, under construction and development as a function of the power capacity. For PTC technology, the CAPEX ranges between 2,380 €/kW and 7,727

€/kW. Note that there is a large variance in investment cost in similar plants in different countries. However, for tower technology, the CAPEX ranges between 1,926 €/kW and 10,045 €/kW. Again, the labour cost also influences the investment cost, as noted when comparing similar CSP plants installed in South Africa or China, although different storage capacities and types also affect the investment cost. In addition, it is difficult to relate power plant capacity and CAPEX because the TES system plays an important role in the initial investment cost.

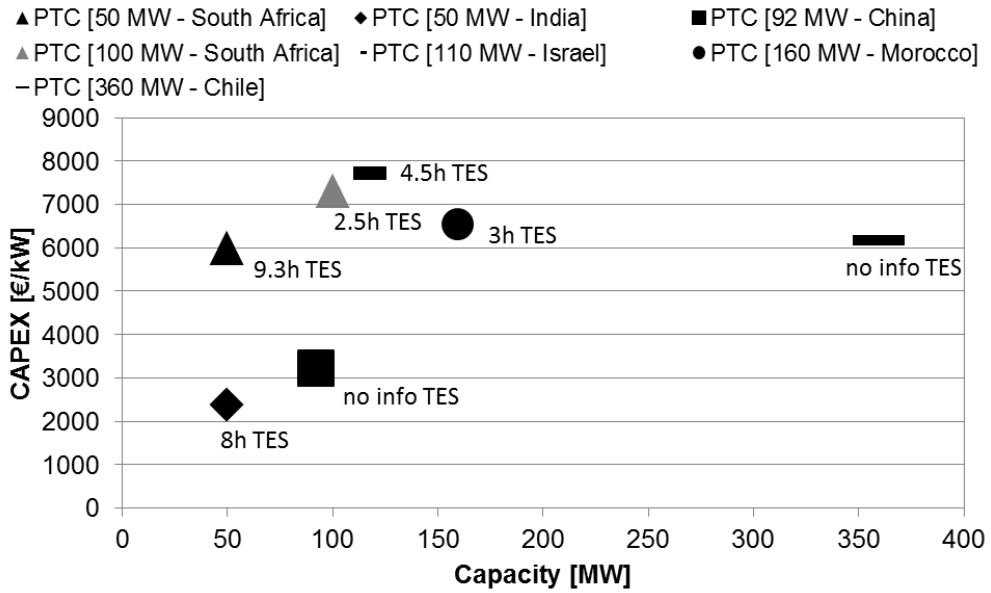

Figure 13. CAPEX for commercial PTC CSP plants under construction and development.

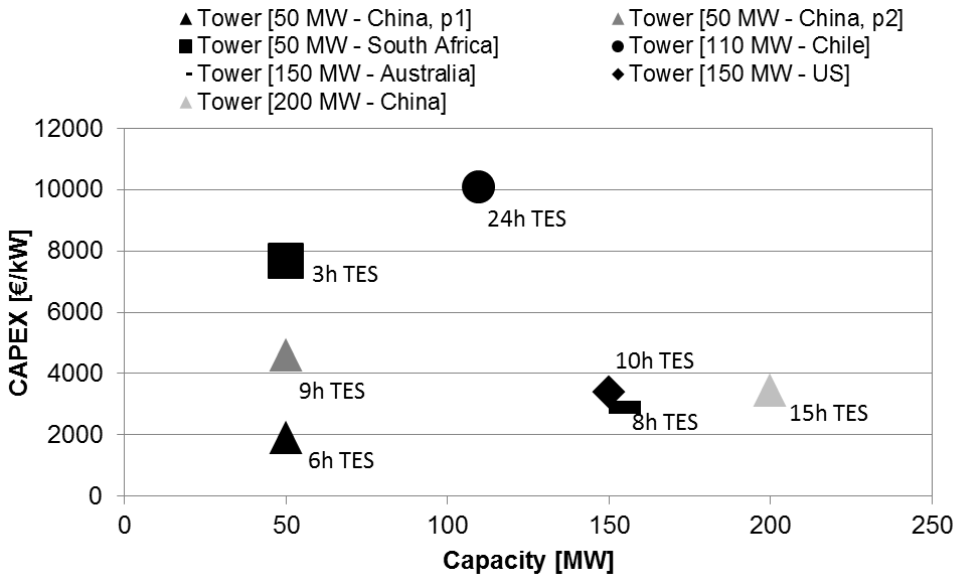

Figure 14. CAPEX for commercial tower CSP plants under construction and development.

Figure 15 shows the investment cost of PTC plants as a function of the power capacity. Note that this CAPEX also considers the storage capacity when evaluating its influence on the total investment cost. All CSP systems analysed include a molten-salt two-tank indirect system as the TES system. Similarly, Figure 16 shows the investment cost for tower plants as a function of the power capacity. In this case, the TES system implemented is a molten-salt two-tank direct system, except for the 50-MW tower CSP plant in South Africa (which has saturated steam as its TES solution).

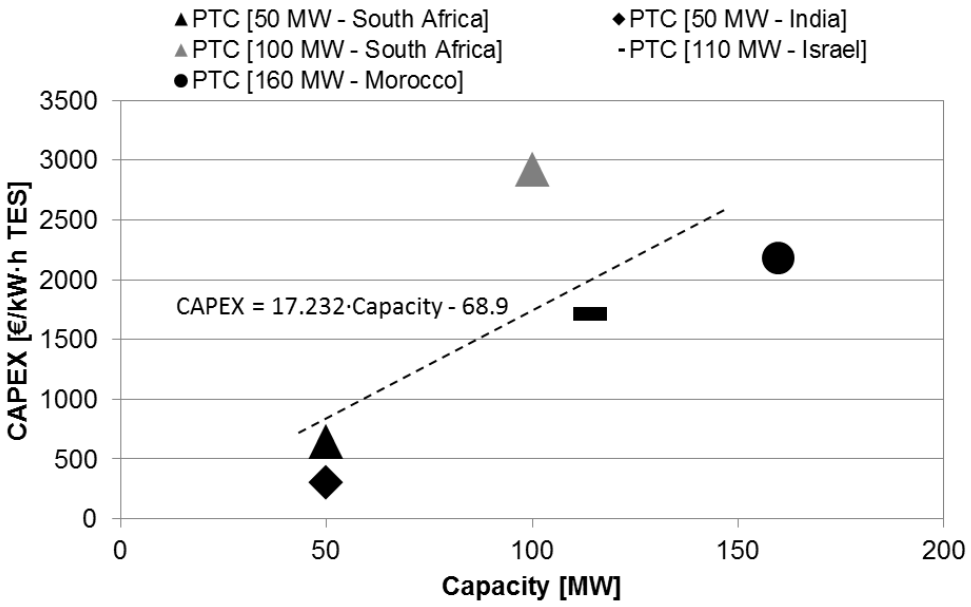

Figure 15. CAPEX for commercial PTC CSP plants with molten salt as TES.

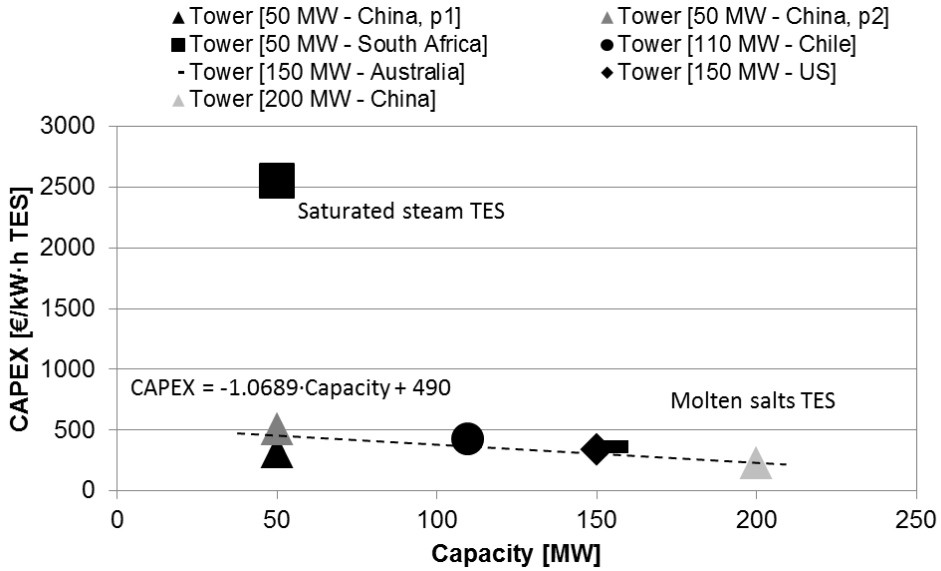

Figure 16. CAPEX for commercial tower CSP plants with molten salt as TES.

With the trend lines calculated using real data from commercial CSP plants, it is possible to estimate current investment costs as a function of the power capacity and storage capacity. Thus, Figure 17 compares the calculated investment costs for PTC and tower CSP plants including six hours of storage capacity with the cost projections of the plants depicted in the IEA report [10]. The present investment cost for tower CSP plants is lower than the projected cost by the IEA for 2020 for different capacity power installed. In

contrast, for PTC CSP plants, the actual investment cost is much higher than that predicted for 2020 for solar plants greater than 50 MWe.

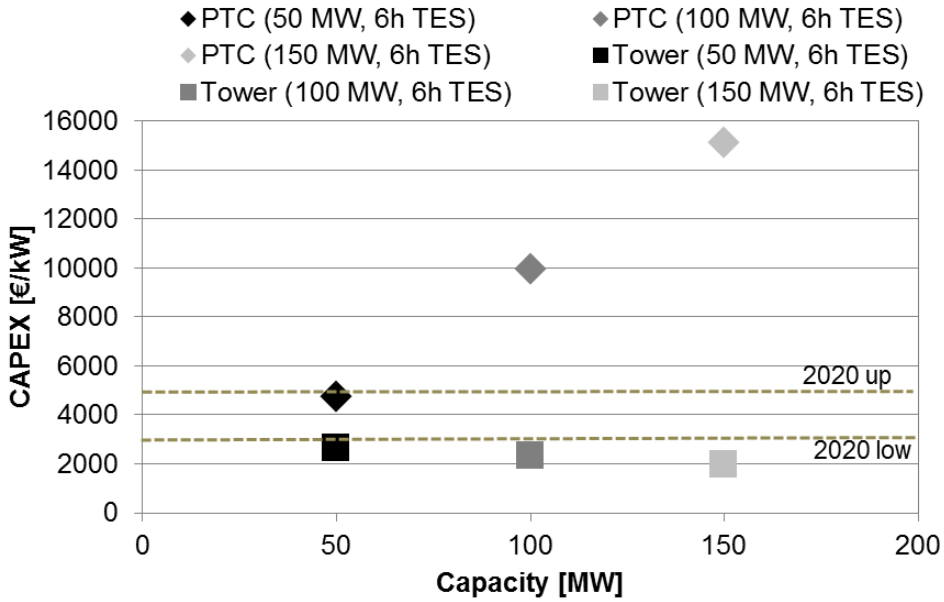

Figure 17. CAPEX for commercial CSP plants with six hours of storage capacity compared to the projected costs by the IEA for 2020.

Most CSP plants costs are incurred upfront, when the power plant is built. Once built, CSP plants can generate electricity virtually for free. Investors therefore need to be able to rely on future revenue streams so that they can recover their initial capital investments. Thus, market structures and regulatory frameworks that fail to provide robust long-term price signals beyond a few months or years are unlikely to attract sufficient investment to achieve expected future CSP integration and timely decarbonisation of the global energy system. An actual strategy to overcome this problem is the power purchase agreement (PPA). The PPA is a contract between two parties, one of which generates electricity (the seller) and the other of which wants to purchase electricity (the buyer). The PPA defines all the commercial terms for the sale of electricity between the two parties, including when the project will begin commercial operation, the schedule for delivery of electricity, the penalties for underdelivery, payments terms, and termination. Many of the current CSP plants under construction and development have signed PPA contracts with other parties as a key instrument of project finance. Figure 18 shows the PPA agreements for different worldwide CSP plants. Current prices (average of 0.165 €/kWh) are much lower than the PPA agreements signed in Spain during the period of maximum growth of CSP

plants, where the standard PPA was 0.3 €/kWh incentivised mainly by the Spanish government. The current trend indicates that the CSP plant is now much more mature, where the cost of electricity production is competitive compared to other renewable and fossil fuel sources.

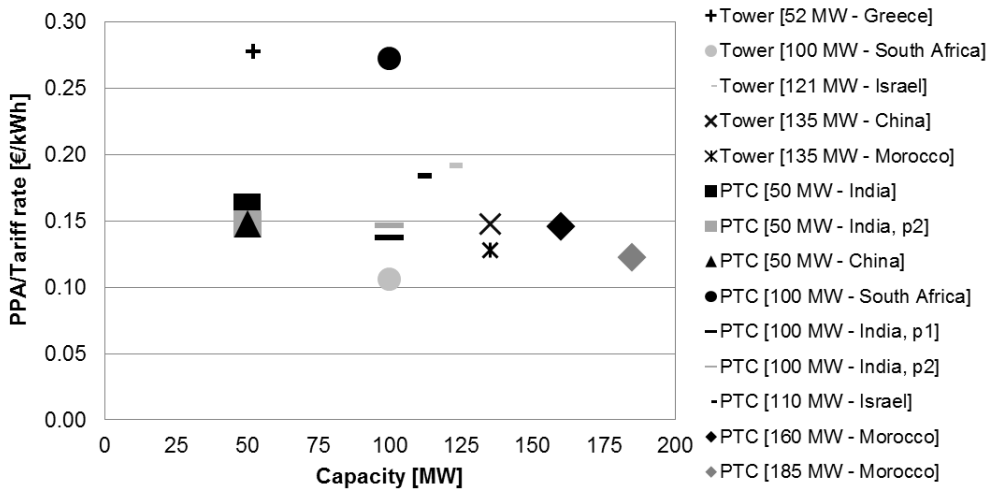

Figure 18. PPA agreement for commercial CSP plants.

1.4. Molten salts in commercial use

TES for CSP systems use a variety of different media, technologies, and sizes. In this section, commercial solar power plants and technologies that use molten nitrate salts for TES will be discussed, along with an historical perspective on the development of nitrate salt specifications.

Commercial solar plants using nitrate salts for TES (Table 1) employ two primary collection technologies: parabolic troughs and power towers (also called central solar receivers). Parabolic troughs are suited to modular deployment because the mirrors and collector are produced in a one-to-one arrangement. As a result, they act as linear concentrators and are capable of achieving roughly 100 suns, with a maximum temperature of ~550°C. Power towers require large heliostat fields for a single receiver because power towers are point concentrators, but they can achieve more than 1,000 suns, with maximum temperatures greater than 2,638°C [11]. Although the higher operating temperatures of a power tower are preferable, their high capital cost has been prohibitive,

resulting in wider use of the lower capital cost, modular parabolic troughs despite their lower operating temperatures.

Named for the parabolic-shaped mirror they leverage, parabolic troughs are designed with the collector located at the mirror focal point. A pipe or tube serves as a collector, and a heat-transfer fluid shuttles the solar heat to the TES medium. HTFs are either a eutectic mixture of diphenyl and diphenyl oxide (i.e., oil) or a molten salt. Most trough systems (Table 1) use diphenyl/diphenyl oxide as the HTF due to the low freezing point of the fluid. Maximum temperature limits on trough systems are a result of the HTF used (diphenyl/diphenyl oxide yield a maximum-use temperature of 400°C) or optical collection limits (~550°C in the case of the Archimede plant).

Power towers are surrounded by heliostats that focus solar energy onto a central receiver, allowing for much higher heat fluxes compared to trough designs. Power tower central receivers have a variety of designs, but all designs are currently limited by the maximum operating temperature of their working fluid. Power towers use 60 wt.% sodium nitrate and 40 wt.% potassium nitrate, called solar salt, as the HTF.

Solar salt was first demonstrated for commercial use during the Solar Two project [12]. The 60/40 $NaNO_3/KNO_3$ ratio was selected to balance requirements for melting point, cost, heat capacity, and viscosity. Solar salt does not have a congruent melting point (the phase diagram is an isomorph) with a liquidus temperature around 240°C and a practical minimum-use temperature of ~290°C set by the liquidus temperature of the salt, plus a 50°C margin, to avoid freezing of the salt. Industry typically assumes that from 565°C the Solar salt degrades into gas and oxide anions, significantly increasing corrosion. Some laboratory data indicate that higher operating temperatures up to 600°C are possible [13]. The higher liquidus point was viewed as an engineering trade-off to decrease mixture cost by increasing the overall composition of $NaNO_3$, which was less expensive during the 1990s. Allowable impurities, as provided in Table 2, were determined by practical engineering considerations and experiments.

Chloride is the key impurity that causes a dramatic change in corrosion performance. Early compatibility work investigated two primary grades of materials. Technical-grade

nitrates with chloride content of 0.1 wt.% were compared against industrial-grade nitrates with chloride content of 0.3 wt.%. Although technical-grade nitrates had superior performance, the performance margin was not sufficient to outweigh the higher cost; therefore, industrial-grade nitrates were selected for Solar Two [14].

In additional experiments, maximum allowable chloride levels were determined through stainless-steel and carbon-steel corrosion performance; these materials are used for piping and storage tanks. The 0.6 wt.% chloride limit, given in Table 2, was set by a mechanism change in stainless-steel corrosion; chloride values above the limit degraded linearly with time, whereas chloride values below the limit exhibited preferable parabolic behaviour [15]. Carbon steels also had improved corrosion performance below this chloride threshold.

Exclusion of nitrite was provided to improve melt stability. Nitrite concentration will slowly accumulate over time through the reaction:

$$\boldsymbol{NO_3^- \rightleftharpoons NO_2^- + \frac{1}{2}O_2} \qquad \text{Eq. 4}$$

This equilibrium reaction was characterized for an equimolar mixture of sodium nitrate-potassium nitrate. The increasing partial pressure of oxygen drives the reaction to favour nitrate [16]. Although both nitrate and nitrite can decompose to a variety of oxide ions (i.e., oxide, peroxide, superoxide), the reaction pathway of sodium/potassium nitrates are primarily to nitrites per Equation 4. Nitrite is a relative marker of melt stability—high nitrite content indicates nitrate decomposition—because nitrite will eventually decompose to metal oxide, nitrogen, and oxygen [17]:

$$\boldsymbol{2NO_2^- \rightleftharpoons O^{-2} + N_2 + \frac{3}{2}O_2} \qquad \text{Eq. 5}$$

N_2 generated through this reaction forms a triple bond between nitrogen atoms and will not be available for a back reaction to nitrites; thus, for all practical purposes, Equation 5 only proceeds from left to right. NO or NO_2 present in the cover gas may promote a back reaction with metal oxides to re-form nitrate or nitrite, where mixtures of these gases could remove oxides from high-temperature melts.

Carbonate concentration limits are provided in the initial salt chemistry, because the carbonate will tend to accumulate in solution over time, as atmospheric carbon dioxide reacts with oxide ions [18]:

$$\boldsymbol{CO_2 + O^{-2} \rightarrow CO_3^{-2}} \qquad \text{Eq. 6}$$

Carbonate concentration in melts may result in unexpected behaviour. However, the primary concern is precipitation of metal carbonates, which can occur in the cold tanks. The solubility limit is several mole percent carbonate in solar salt (K_2CO_3 in KNO_3 ~3 mol% at 326°C, Na_2CO_3 in $NaNO_3$ is ~2 mol% at 307°C [19]). Carbonate accumulation could result in insoluble products that may eventually lead to plugging or erosion within the system, although this has not been observed to the authors' knowledge.

Hydroxyl ions are another oxidizing agent capable of corroding metals via the following reaction [20]:

$$\boldsymbol{M + xOH^- \rightarrow MO_x + \frac{x}{2}H_2} \qquad \text{Eq. 7}$$

Metal oxides and hydrogen are formed as by-products of the reaction. Minimizing oxidizers, e.g., hydroxyl ions, should reduce corrosion of structural metals. Based on phase diagrams, hydroxide appears to be readily soluble in solar salt, and it should be removed during salt production.

Sulphate ions can cause a variety of different corrosion problems and have played a significant role in fireside corrosion, as observed in coal plants [21,22]. Corrosion with 7.5 wt.% of Na_2SO_4 resulted in a corrosion rate increase of about 20% [23]. Furthermore, limiting the amount of sulphate should preclude the formation of a variety of low-melting point (550°–565°C) metal-iron-trisulphates that could contribute to accelerated attack. Nitrate melts do not significantly increase their corrosive behaviour with additions of sulphate above 0.75 wt.%, a formulation that balances cost and purity.

One of the key lessons learned during the Solar Two project was the necessity of minimizing magnesium. Although present in only small quantities—0.045% in the form of $Mg(NO_3)_2$ as given in Table 2—upon reaching temperatures of ~480°C, the following reaction occurred [12]:

$$2Mg(NO_3)_2 \rightarrow 2MgO_{(s)} + 4NO_{2(g)} + O_{2(g)} \quad \text{Eq. 8}$$

The evolution of nitrogen dioxide is a serious concern due to its relative toxicity. The Solar Two project dealt with this reaction using a series of isothermal holds, with nitrogen oxides being diluted with ambient air and then released up a 30-foot stack [14]. This had not been previously observed, but given the experience at Solar Two, subsequent projects include the recommendation for low magnesium concentrations. A recent study by Prieto et al. [24] shows how although the impurity magnesium nitrate is the main source of NOx emissions during the commissioning of the plant due to its thermal decomposition during the melting process, this NOx production can be handled by vents and abatement systems if it is needed [24].

Table 1. Operational solar power plants using solar salt for thermal energy storage [25]

Plant	**Technology**	**Temperature Range [ºC]**	**Storage [Hours]**	**Turbine Capacity [MW]**	**Heat-Transfer Fluid**
Gemasolar Thermosolar Plant	Power tower	290–565	15	20	Solar salt
SunCan Dunhuang	Power tower	290–565	15	10	Solar salt
Crescent Dunes	Power tower	290–565	10	110	Solar salt
Andasol-1, 2, 3	Parabolic trough	293–393	7.5/plant	50/plant	Diphenyl/diphenyl oxide
Archimede	Parabolic trough	290–550	8	5	Solar salt
Arcosol 50	Parabolic trough	293–393	8	49.9	Diphenyl/diphenyl oxide
Arenales	Parabolic trough	293–393	7	50	Diphenyl/diphenyl oxide
Aste 1A/1B	Parabolic trough	293–393	8/plant	50/plant	Diphenyl/diphenyl oxide
Astexol II	Parabolic trough	293–393	8	50	Diphenyl/diphenyl oxide
Bokpoort	Parabolic trough	293–393	9.3	55	Diphenyl/diphenyl oxide

Casablanca	Parabolic trough	293–393	7.5	50	Diphenyl/diphenyl oxide
Extresol-1, 2, 3	Parabolic trough	293–393	7.5/plant	50/plant	Diphenyl/diphenyl oxide
KaXu Solar One	Parabolic trough	293–393	2.5	100	Diphenyl/diphenyl oxide
La Africana	Parabolic trough	293–393	7.5	50	Diphenyl/diphenyl oxide
La Dehesa	Parabolic trough	293–393	7.5	50	Diphenyl/diphenyl oxide
La Florida	Parabolic trough	293–393	7.5	50	Diphenyl/diphenyl oxide
Manchasol-1, 2	Parabolic trough	293–393	7.5/plant	50/plant	Diphenyl/diphenyl oxide
NOOR I	Parabolic trough	293–393	3	160	Diphenyl/diphenyl oxide
Solana Generating Station	Parabolic trough	293–393	6	280	Diphenyl/diphenyl oxide
Termesol 50	Parabolic trough	293–393	7.5	50	Diphenyl/diphenyl oxide
Termosol 1, 2	Parabolic trough	293–393	9/plant	50/plant	Diphenyl/diphenyl oxide
Xina Solar One	Parabolic trough	293–393	5.5	100	Diphenyl/diphenyl oxide

Table 2. Salt specification for Solar Two and actual composition of salt upon reception [12].

Parameter	**Specification**	**Solar Two Actual**
$NaNO_3$:KNO_3 wt.% ratio	60:40	58:42
Total chloride concentration	0.6 wt.%	Chloride 0.36%, perchlorate 0.26%
Nitrite	1 wt.%	0
Carbonate	0.10 wt.%	23.4 ppm
Sulphate	0.75 wt.%	0.12%
Hydroxyl	0.20 wt.%	0
Minimum 98 wt.% nitrate salt	–	–
Calcium	N/A	45 ppm
Magnesium	N/A	0.045%
Chromium	N/A	0

2. Thermal properties required for TES in CSP

The materials implemented in CSP to store thermal energy should be previously characterized. The characterization is based on obtaining their thermophysical properties in the operational range. The main thermophysical properties desired for TES materials in CSP are the following: specific heat, thermal conductivity, melting/solidification enthalpy and temperature, and viscosity. However, other properties such as degradation temperature, thermal stability, density, vapour pressure, and thermal expansion coefficient are necessary when looking for TES materials and designing the CSP plant implementing those materials. Each property can be experimentally obtained by a measurement technique which might correspond to a commercial technique. Sometimes the desired property is also available in the literature, but in this case, one needs to evaluate if the given properties were obtained under the same operating conditions (e.g., heating rate, temperature range) and with acceptable accuracy for further simulations and design.

Specific heat capacity (Cp) is a key factor of the storage/transport system in a solar thermal power plant because this phenomenon completely controls the capacity of rise in temperature that can be stored or transported. Increasing the specific heat capacity increases the overall cycle efficiency [26]. The most widely used technique to measure Cp is differential scanning calorimetry (DSC), and the ASTM 1269E is the most extended procedure to determine the specific heat of a material by DSC [27]. However, it should also be mentioned that new methodologies are arising to improve the accuracy and reduce the scattering of the results [28,29]. A round-robin test (RRT) was performed in the framework of SolarPACES Task III: Solar Technology and Advanced Applications, Thermal Energy Storage Working Group. The specific purpose of the RRT was to determine and compare the Cp of the solar salt between several partners. The preliminary results show that the normalized method ASTM E1269 and modulated DSC (MDSC^{TM}) [30] are adequate for measuring Cp of the solar salt in the temperature range between 200ºC and 400ºC [31].

Solidification/melting temperature is another key thermal property of the TES materials for CSP, and it is directly related to operational costs. A high melting point results in more

operations and maintenance costs due to freezing protection because additional heat is required to keep the solar-field temperature above the HTF melting/solidification point even at night [26]. The DSC is also used to obtain the melting/solidification temperature. A standard methodology was developed to determine the phase-change enthalpy (also known as latent heat or heat of fusion) of phase-change materials (PCMs) using DSC with constant heating/cooling rate (dynamic mode) in the framework of the International Energy Agency (IEA) SHC/ECES T42A29 [32].

Another technique that is not commercially available, but is being used in laboratories, to measure phase-change enthalpy and temperature is the T-history technique [33]. This technique was developed in 1999 mainly for PCM characterization.

In a CSP plant, the higher the operating temperature, the higher the overall efficiency. So, the property that plays a key role is the degradation temperature of the storage media. The thermal decomposition (degradation) temperature refers to the value at which the sample has lost 3 wt.% compared to the initial weight [34]. The thermogravimetric analysis (TGA) technique can determine the degradation temperature. A thermogram of mass loss as a function of temperature is obtained, from which can be calculated the percentage of mass loss of the sample (molten salt in this case) as a function of temperature. This approach must be performed during an extended period of time under isothermal temperatures.

TGA can also be used to study the thermal stability of a given sample—for example, to study how the sample behaves under different atmospheres, such as oxygen, nitrogen, argon, or mixtures. Bauer et al. [35] studied the thermal stability of $NaNO_3$ and solar salt; specifically, the authors measured the influence of the partial pressure of oxygen on the thermal stability. Their results confirm a stabilizing effect by increased oxygen partial pressure in open-system-type experiments with nitrogen-oxygen atmospheres. In addition, TGA measurement also allows knowing if side reactions, usually undesired, are occurring.

Thermal stability can also be studied by using an oven and keeping the samples at a certain temperature (and also, if desired, under different atmospheres). The analysis is based on comparing the sample before and after the oven tests. The sample can be

analysed by a chemical analysis technique, such as infrared spectroscopy (IR), looking for any changes in the chemical composition, and/or by a thermal analysis technique (such as DSC) to see if there is any change in the phase-change temperature or enthalpy. This procedure is more commonly used to study PCM cycling thermal stability, and thus, uses the oven to cycle the PCM from below to above its melting temperature [36].

For the thermal conductivity (k) measurement, the most commonly used method is the steady-state method, in which the material is placed in a cylindrical container and temperature gradient is measured to calculate k [37]. The laser-flash technique is also quite commonly used to measure k of molten salts [38], being an indirect measurement. In fact, thermal diffusivity is the measured property with laser flash technique, and with Eq. 9, thermal conductivity can be calculated:

$$k = a \cdot \rho \cdot Cp \qquad \text{Eq. 9}$$

where, a is the thermal diffusivity, ρ is the density, and Cp is the heat capacity [35].

Other methods used for molten-salt k measurements are coaxial cylinders made of platinum with radiation heat transfer [37], a transient plane-source (TPS) sensor, and based k analyser [39].

Knowing the viscosity (dynamic viscosity) of the molten salt is desired mainly because it affects the energy consumption required to pump it. A rheometer, usually a dynamic shear rheometer, is needed to measure the viscosity at certain temperature points and shear rates. Viscosity of molten salts depends considerably on temperature; therefore, enough measurements are required from above its melting/freezing point to the operating conditions. Note that rheological parameters—shear stress, deformation, and shear rate—are calculated from the measured values—torque, deflection angle, and speed, respectively—using conversion factors. All further parameters, such as viscosity, are not measured but calculated.

Density, as well as thermal conductivity, is very sensitive to temperature. Therefore, it is highly recommended to measure it in the operating temperature range. A wide variety of methods are available for density measurement, i.e., hydrometers, pycnometers, digital

density meters, and hydrostatic balances. Note that some density-measurement methods determine apparent density (weight per volume) whereas others measure true density (mass per volume). Peng et al. [40] studied the density of molten salts by Archimedes theory in an RSD-06 synthetic test instrument.

Another thermophysical parameter required to fully characterize molten salts is vapour pressure. To implement these materials in CSP, low vapour pressure is favourable because it indicates liquid evaporation rate. Empirical methods are used to calculate the vapour pressure. The Antoine equation can be used to calculate the vapour pressure as a function of temperature or Clausius-Clapeyron equation if the heat of fusion is known [41]. Moreover, several measurement techniques are available, such as the Knudsen cell technique [42] and TGA [43].

The thermal-expansion coefficient of several molten salts was investigated by Peng et al. [40] with a thermal-expansion instrument. Also, Meffre et al. [44] studied the thermal-expansion behaviour of TES materials using a commercial dilatometer. The volumetric expansion is interesting to consider in designing CSP because the expansion has the potential to damage system components as well as the volumetric change when recovering from freezing, because it can fracture the piping.

Other requirements, in addition to the thermophysical properties required for TES in CSP, would be the optical properties [32], cost of the TES material (see Section 1.3), environmental impact, corrosion studies [33], and flammability.

3. New molten salts proposed

3.1. Ternary/quaternary molten nitrates/nitrites

During the last several years, new molten salts proposed to be applied as HTF and/or TES in CSP plants have been studied extensively [45–47]. In the 1990s, patents emerged for new additives and mixtures for CSP technology plants [48].

The potential for improving the salt resides in optimising its physicochemical properties—mainly its melting point, thermal stability, and heat capacity—by developing

new ternary or quaternary mixtures, with the aim of improving the work temperature range. Heat capacity improvements will be discussed in the following section as well as an update of the studies involving the addition of nanoparticles. Michel et al. [48] proposed the mixture composed by 44 wt.% $Ca(NO_3)_2$ + 44 wt.% KNO_3 + 12 wt.% $NaNO_3$, with the main drawback being its high viscosity.

Several authors [49,50] reported the importance of controlling the $NaNO_3$ content in ternary salts because it is responsible for the viscosity of the mixture. Taking these characteristics into account, the authors proposed a 60 wt.% KNO_3 + 22 wt.% $LiNO_3$ + 18 wt.% $Ca(NO_3)_2$ mixture, which has a melting point of 112°C and reasonable viscosity values. Kniep and Lotz filed patents [51,52] proposing mixtures of $LiNO_3$ and $Mg(NO_3)_2*6H_2O$, in which the eutectic mixture 83.7 wt.% $Mg(NO_3)_2*6H_2O$ + 16.3 wt.% $LiNO_3$ is notable, with a melting point of 75.6°C, as determined by DSC.

In 2000, Lotz et al. [52] proposed the mixture $Mg(NO_3)_2*6H_2O$ + $LiNO_3$, introducing KNO_3 or $NaNO_3$, which has a low melting point (55°C) and a high melting enthalpy; its main drawback is its lower thermal stability. Mixtures proposed in CSP technology have primarily focused on ternary and even quaternary formulations of alkaline nitrates/nitrites that have energy-storage functions in an attempt to improve the melting point of solar salt and the control of its impurities. Raade et al. [34] presented mixtures with up to five components and diverse compositions. They introduced cesium nitrate to mixtures known from the literature, succeeding in reducing the melting point to 70ºC. However, the cost of $CsNO_3$ (which is even higher than $LiNO_3$) makes these mixtures commercially unviable. The same researchers designed new formulations chosen from among thousands of compositions that reduce the melting point to below 60ºC [54]. The use of nitrite as a salt component was also proposed because it could increase the thermal stability of salts. The thermal properties of the Hitec mixture, a molten salt composed of 40 wt.% $NaNO_2$ + 7 wt.% $NaNO_3$ + 53 wt.% KNO_3, are highly suited to its use as a storage fluid in CSP plants [55]. One disadvantage of this mixture is the need to use an inert gas at temperatures above 350ºC to avoid oxidation of the nitrites upon contact with oxygen in the atmosphere [56,57]. This is the main reason that presently prevents the widespread use of this salt on CSP plants; however, several research projects are currently seeking to improve the physical properties of the mixture to a point in which the mixture's enhanced properties could compensate its higher costs.

The literature shows that it is clear that adding $Ca(NO_3)_2$ or $LiNO_3$ could improve the working temperature range as well as the corrosion resistance in the container materials in contact with these ternary mixtures [58,59]. For $Ca(NO_3)_2$, its low cost and ability to reduce the melting point of alkaline nitrates demonstrate the potential of the additive to be included in new formulations of molten salts for energy storage; it is a feasible candidate to replace the synthetic oils used in parabolic trough technology as HTF. Bradshaw et al. [60] studied different additions of $Ca(NO_3)_2$ to the binary salt $NaNO_3/KNO_3$, analysing the concentration of nitrites in different mixtures at temperatures between 350ºC and 530°C. Gomez et al. [61] reported the handling, preparation, thermal properties, and characterization of different compositions for this ternary nitrate salt. The authors concluded that this ternary system has a high tendency to form supercooled liquids with high viscosity that undergo glass formation during cooling, not recommending its use up to 520ºC.

Another one of the most studied additives for energy storage is lithium nitrate. Siegel et al. [18] highlighted its suitable characteristics for improving the operation temperature range of salts, although its main problem is cost. Regarding this drawback, Fernandez et al. [59] proposed a method for obtaining this $LiNO_3$ from brines present in the Atacama Desert that would help reduce the final cost of this additive. The most notable property of the molten salts using lithium nitrate is energy density (based on heat capacity and density), which represents an important improvement over the solar salt currently used. Based on this parameter, smaller volumes of the proposed salt could be used to store the same amount of energy. Parrado et al. [62] established the levelized cost of energy (LCOE) projection in this kind of ternary salt, obtaining a reduction of about 30% with a final cost of about 7.35 ¢USD/kWh for the CSP plant. The addition of lithium nitrate to the solar salt is assumed to improve the performance of molten salts, extending the temperature work range regarding its low melting point, which, in the short term, can be profitable despite the higher cost of operating plants with these fluids.

The first study documenting the eutectic point of the $LiNO_3/NaNO_3/KNO_3$ mixture dates back to 1964 [63], when it was determined that the 17.3 wt.% $NaNO_3$ + 59.4 wt.% KNO_3 + 23.3 wt.% $LiNO_3$ composition has the lowest melting point. Xu et al. [64] predicted a eutectic temperature of 98.3ºC for a quaternary system composed of 9.5 mol% $NaNO_3$,

52.8 mol% KNO_3, 27.6 mol% $LiNO_3$ and 10.1 mol% $Ca(NO_3)_2$. However, the main drawback for this mixture is the lower thermal stability, fixed at 450ºC. In a recent study, Wang et al. [65] established the eutectic composition for 25.9 wt.% $LiNO_3$ + 20.6 wt.% $NaNO_3$ + 54.1 wt.% KNO_3 mixtures, but Olivares et al. [66] determined the eutectic composition for 30 wt.% $LiNO_3$ + 18 wt.% $NaNO_3$ + 52 wt.% KNO_3 using Factsage software. Consequently, proper preparation, mixing, and handling of the salts is important to obtain reproducible results. In preparing different homogenous ternary molten salts for CSP applications, Pramod at al. [39] established a new methodology using a closed pressure vessel. The hydrated salt in the mixture liberates water inside the closed vessel, and molten salt results that is homogenous under mild conditions.

In addition to studies by Mantha et al. [67], Wang et al. [68], Ren et al. [69], and Mehedi et al. [70] involving the addition of $Ca(NO_3)_2$ and $LiNO_3$, Fernandez et al. [71] proposed a quaternary molten salt containing 10 wt.% $LiNO_3$ + 20 wt.% $NaNO_3$ + 60 wt.% KNO_3 + 10 wt.% $Ca(NO_3)_2$. This quaternary mixture was designed taking into account the commercial requirements of the solar energy market and storage cost objectives. Therefore, the maximum content of $LiNO_3$ and $Ca(NO_3)_2$ does not exceed 10% because of the material's high cost and limitations associated with working at high temperatures.

As mentioned previously, these ternary/quaternary molten salts with low melting point were proposed as HTF and TES, mainly in parabolic trough solar power plants, replacing the synthetic oil currently used as HTF. This configuration was developed by ENEA and is already used in the Archimede plant in Priolo Gargallo (Sicily, Italy). Sau et al. [72] performed a techno-economic comparison between solar salt and a ternary salt composed by 37/45/18 mol.% of $NaNO_3$/KNO_3/$LiNO_3$. The authors concluded that the main advantage of using a ternary salt is the lower melting point, allowing a reduction in the average temperature of the solar field during periods without solar radiation; hence, this led to thermal dispersions about 80% lower compared with solar salt. However, the binary mixture is significantly less expensive than the ternary one and it can compensate the minor backup power required that is related to the minor heat losses in ternary salts. The density of these ternary salts containing $LiNO_3$ was reported by Janz et al. [73] using data from the literature. However, Nissen [74] and Zavoico [75] used the Archimedean method for the calculation. Bauer et al. [76] proposed an equation relating the density (ρ) and

temperature (T) according to data available in the literature. This equation is the following:

$\rho\ (g/cm^3) = 2.1060 - 6.6795 \cdot 10^{-4}\ T\ (^oC)$. Eq. 10

Results available in literature agree with the proposed equation. Gonzalez-Roubaud et al. [8] analysed the potential use of ternary salts such as Hitec and Hitec XL as HTF in CSP plants replacing the solar salt. The authors concluded that the maximum operation temperature is significantly lower than solar salt. Hitec is thermally stable at temperatures up to 454ºC, and it could be tested at temperature up to 538ºC. On the other hand, authors do not recommend using Hitec XL up to 500ºC because of the quick decomposition of $Ca(NO_3)_2$ to calcium oxide.

In this area, some authors have studied the influence of different impurity contents on storage properties. Fernandez et al. [58] concluded that the water content present in calcium nitrate salts also contributes to decrease its melting point, given that the registered melting point for this pure nitrate (without water) is 561°C. This feature should help lower the melting point of ternary mixtures containing calcium nitrate tetrahydrate. Brockner et al. [77] studied water loss in calcium nitrate tetrahydrate and detected the following water-loss reactions at the indicated temperatures:

$$Ca(NO_3)_2 \cdot 4H_2O \Leftrightarrow Ca(NO_3)_2 \cdot 3H_2O + H_2O \text{ at } T = 45°C$$

$$Ca(NO_3)_2 \cdot 3H_2O \Leftrightarrow Ca(NO_3)_2 \cdot 2.5H_2O + 0.5H_2O \text{ at } T = 67°C$$

$$Ca(NO_3)_2 \cdot 2.5H_2O \Leftrightarrow Ca(NO_3)_2 + 2.5H_2O \text{ at } T = 154°C$$

$$Ca(NO_3)_2 \Leftrightarrow CaO + N_2O_5,$$

$$\text{where } N_2O_5 \Leftrightarrow 2NO_2 + 0.5O_2 \text{ at } T = 532°C.$$

Paulik et al. [78] also studied the decomposition of calcium nitrate and observed sequential water loss at 49°C, 120°C, 160°C, and 210°C. In a recent work, Grosu et al. [79] established the influence of humidity and impurities in the corrosive potential of Hitec XL as a storage material in a thermocline TES system. Corrosion rates obtained agreed with the literature, and the authors reported on the influence of humidity in the corrosion process. Fernandez et al. [80] also reported this influence in a previous work, along with the corrosive impurities present in solar salt. These results will be used for selecting materials in the commercial project of a 1-MWe pilot plant at Green Energy

Park in Ben Guerir (Morocco). Table 3 shows the ternary/quaternary molten nitrates/nitrates that have been widely studied in the literature, including the main important thermal properties.

Another parameter to highlight is the maximum operation temperature in ternary/quaternary molten nitrates/nitrates. A validated test for determining the maximum working temperature does not exist in the literature. One approach is to set this maximum temperature when the salt has lost 3 wt.% of its initial mass (after weight stabilization due to water loss). Fernandez et al. [81] developed some isothermal tests at these temperatures, determining that mass loss still occurs over time assuming that the decomposition in the salts continues once they have begun the decomposition process.

Some authors are proposing that the maximum work temperature for CSP molten-salt technology should be set at the onset of the TGA curve. This consideration has been considered for thermal stability evaluation shown in Table 3.

Table 3. Main ternary/quaternary molten salts proposed in literature as TES material

Heat transfer and storage material (wt.%)	Melting point (°C)	Thermal stability (°C)		Viscosity (Pa·s)	Heat capacity (J/g·°C)	Thermal conductivity (W/m·K)	References
		Onset T (°C)	3wt.% loss (°C)				
60%$NaNO_3$ + 40%KNO_3	220	485.68	588.51	0.00326 (at 300ºC)	1.52 (at 390ºC)	0.55 (at 400ºC)	[47,81]
40%$NaNO_2$ + 7%$NaNO_3$ + 45%KNO_3	142	535	600	0.00316 (at 300ºC)	1.56 (at 300ºC)	0.2 (at 300ºC)	[47,75,58]
48%$Ca(NO_3)_2$ + 7%$NaNO_3$ + 45%KNO_3	120	423	554	0.00637 (at 300ºC)	1.45 (at 300ºC)	0.52 (at 300ºC)	[47,75,58]
20%$LiNO_3$ + 28%$NaNO_3$ + 52%KNO_3	130	514	600	0.03 (at 300ºC)	1.091 (at 300ºC)	N.A.	[47,58]
30%$LiNO_3$ + 10%$Ca(NO_3)_2$ + 60%KNO_3	132	477	567	0.002 (at 300ºC)	1.39 (at 390ºC)	N.A.	[58]
17.8%$NaNO_2$ + 17.5%$LiNO_3$ + 14.2%$NaNO_3$ + 50.5%KNO_3	99	N.A.	430	N.A.	1.66 (at 500ºC)	N.A.	[47]
19%$Ca(NO_3)_2$ + 8%$LiNO_3$ + 6%$NaNO_3$ + 23%KNO_3 + 44%$CsNO_3$	65	N.A.	500	N.A	1.22 (at 150ºC)	N.A.	[47]
20%$NaNO_3$ + 10%$LiNO_3$ + 10%$Ca(NO_3)_2$ + 60%KNO_3	132	469	580	0.013 (at 300ºC)	1.52 (at 390ºC)	N.A.	[71]
10%$NaNO_3$ + 20%$LiNO_3$ + 10%$Ca(NO_3)_2$ + 60%KNO_3	107.7	N.A.	>500	0.005 (at 300ºC)	1.5 (at 300ºC)	0.54 (at 300ºC)	[69]
15%$NaNO_3$ +18%$LiNO_3$ +31%2KNO_3*$Mg(NO_3)_2$ + 36%KNO_3	102.3	N.A.	N.A.	N.A.	1.67 (at 500ºC)	N.A.	[65]
14%$NaNO_3$ + 18%$LiNO_3$ + 18%$NaNO_2$ + 50%KNO_3	94.3	430	500	N.A.	1.66 (at 500ºC)	N.A.	[68]
29.6%$LiNO_3$ + 13.2%$NaNO_3$ + 57.2%KNO_3	123	N.A.	533	N.A.	N.A.	N.A.	[70]

Bauer et al. [76] established the relationship between the anions (nitrate and nitrite) along with the different cations used in literature (Ca, K, Li, and Na). See Table 4.

Table 4. Melting points depending on the nitrate/nitrite anions relationship for Ca, K, Li, and Na cations

Single and binary system with common cation	**NO_2**	**NO_3**	**NO_2-NO_3**
Ca	398ºC	561ºC	393ºC
K	440ºC	334ºC	316–323ºC
Li	220ºC	254ºC	196ºC
Na	275ºC	306ºC	226–233ºC
Binary system with common anion and ternary reciprocal	**NO_2**	**NO_3**	**NO_2-NO_3**
Ca,K	185ºC	145–174ºC	130ºC
Ca,Li	205–235ºC	235ºC	178ºC
Ca,Na	200–223ºC	226–230ºC	154ºC
K,Li	98ºC	126ºC	94ºC
K,Na	225ºC	222ºC	142ºC
Li,Na	151ºC	196ºC	126ºC
Ternary additive common anion and quaternary reciprocal	**NO_2**	**NO_3**	**NO_2-NO_3**
Ca,K,Li	N.A.	117ºC	N.A.
Ca,K,Na	N.A.	130ºC	N.A.
Ca,Li,Na	N.A.	170ºC	N.A.
K,Li,Na	N.A.	119ºC	75ºC
Quaternary additive common anion and quinary reciprocal	**NO_2**	**NO_3**	**NO_2-NO_3**
Ca,K,Li,Na	N.A.	109ºC	N.A.

3.2. Addition of nanoparticles to molten salts

One of the latest attempts to enhance heat transfer and energy efficiency of CSP plants is to add nanoparticles to molten salts, also known more generally as nanofluids. In general terms, nanofluids can be defined as a new class of advanced HTFs that are engineered by dispersing nanoparticles (particle sizes smaller than 100 nm) in conventional HTFs [26]. The primary aim of these nanofluids is to maximize either the thermal conductivity and/or the specific heat capacity, while simultaneously minimizing their effect on viscosity. The

addition of nanoparticles may affect other material properties that have also been evaluated, such as the phase-change enthalpy [83] and corrosion/erosion. Depending on the base fluid, the effect of adding nanoparticles might even have detrimental results. As shown in Figure 19, molten salts as the base fluid offer higher changes in specific heat capacity than other base fluids with nanoparticles such as ionic liquids, water, or ethylene glycol and mixtures. Therefore, molten salts are appropriate materials in which to add nanoparticles so as to enhance their specific heat.

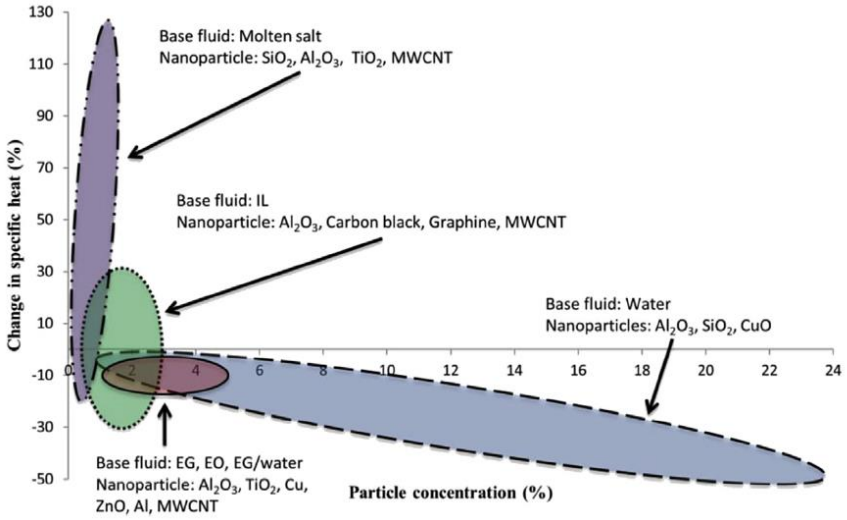

Figure 19. Overview of change in specific heat of different nanofluids grouped by base fluid vs. particle concentration. MWCNT: multi-walled carbon nanotubes, IL: ionic liquids, EG: ethylene glycol [84].

By the theoretical approach proposed by Buongiorno [85], the specific heat capacity of nanofluids should be slightly lower than that of the pure molten salt. In contrast, this is not the case experimentally; rather, the specific heat is enhanced upon doping of nanoparticles to the base eutectic. Hence, this observed enhancement in specific heat capacity cannot be explained by conventional macroscale heat transfer and the theoretical model fails here [26]. Several studies are being published that suggest analytical models to explain this phenomenon. Hentschke [86] reviews the possible theories behind the enhanced specific heat capacity in nanofluids and suggests a model that assumes that the influence of the nanoparticles in the surrounding liquid is of long range. The author adds that the attendant long-range interfacial layers may interact with each other upon increase of nanoparticle concentration. From [87], it is concluded that the primary reason for the enhanced specific heat capacity is assumed to be due to the compressed phase of the

solvent molecules at the solid/liquid interface of the nanoparticles. The evidence for this hypothesis is from experimental results on specific heat capacity values in the solid phase of samples undergoing phase change. The values were observed to be enhanced by 10% compared to values of samples not subjected to phase change.

It is well known from experimental published studies concerning nanofluids development and characterization that several parameters may affect the percentage of enhancement of either thermal conductivity, specific heat, and/or enthalpy. These parameters are primarily the following: nanoparticle mass concentration, nanoparticle size, nanoparticle shape, dispersion (clustered or well-dispersed), and synthesis procedure (at lab scale, one-step, two-steps, dispersion, drying, industrial synthesis, synthesis of the nanoparticles, or commercially available). In addition, the behaviour cannot be extrapolated to all molten salts because there is no pattern. Therefore, each salt and nanoparticle combination should be studied experimentally.

Moreover, measurement techniques have a key role in thermophysical characterization of the nanofluids, and the methodology should be clearly detailed to be able to reproduce measurements. In addition to the required thermal properties described in Section 2 for TES materials in CSP, DSC and TGA are techniques, among others, that are widely used in the nanofluids characterization field at lab scale. Scanning electronic microscopy (SEM) can observe at microscopic scale the presence of nanoparticles and their dispersion, especially when it is coupled with energy-dispersive spectrometry (EDS); this is because the presence of nanoparticles can then be corroborated by chemical analysis, rather than visual inspection only. Another property that is also essential to analyse is particle size or particle-size distribution. This can be evaluated by the dynamic light-scattering (DLS) technique or by SEM (although this is less accurate).

Results and the main characteristics of the experimental studies, whose aim was to enhance either Cp and/or k of a molten salt, are consolidated in five groups according to the base fluid.

75 Table 5. Review of nanofluids based on molten salts along with the main characteristics and results. Cp in [J/g·K], k in [W/m·K]

Base fluid (molten salt)	Nano-particle	Concentration (wt.%)	Nanofluid synthesis procedure	Measurement techniques	Property (% enhancement)	Diameter (nm) and shape	Remarks	Reference
Solar salt ($NaNO_3$-KNO_3, (60-40 wt.%))	SiO_2	1	Twin screw micro-compounder, different mixing time and screw speed	SEM, DSC	Cp_{liquid}: 1.173–1.675 (-28.1–2.6%)	7	Cp values vary as a function of procedure synthesis. Particles aggregation in solid phase was observed	[82]
	Al_2O_3				Cp_{liquid}: 1.505–1.677 (-7.8–2.8%)	13		
	SiO_2/Al_2O_3				Cp_{liquid}: 1.691–1.936 (3.6–18.6%)	2–200		
	SiO_2	0.5	Aqueous solution + sonication + drying in hot plate	SEM, DSC	Cp_{liquid}: 1.329 (-19.3%)	7	The observed enhancement is suggested to be due to the high specific surface energies associated with the high surface area of the nanoparticles per unit volume	[97]
		1.0			Cp_{liquid}: 1.661 (0.8%)			
		1.5			Cp_{liquid}: 1.624 (-1.4%)			
	Al_2O_3	0.5			Cp_{liquid}: 1.522 (-7.6%)	13		
		1.0			Cp_{liquid}: 1.745 (5.9%)			
		1.5			Cp_{liquid}: 1.590 (-3.5%)			
	TiO2	0.5			Cp_{liquid}: 1.390 (-15.6%)	20		
		1.0			Cp_{liquid}: 1.544 (-6.3%)			
		1.5			Cp_{liquid}: 1.454 (-11.8%)			
	SiO_2/Al_2O_3	0.5			Cp_{liquid}: 1.525 (-7.5%)	7/13		
		1.0			Cp_{liquid}: 2.018 (22.5%)			
		1.5			Cp_{liquid}: 1.673 (1.5%)			
	SiO_2	1	Aqueous solution + sonication + drying in hot plate	SEM, DSC	Cp_{liquid}: 1.59±0.03 (10%)	5	It is unclear why the amount of nanostructure formations increases with nanoparticle size	[88]
					Cp_{liquid}: 1.62 ± 0.05 (13 %)	10		
					Cp_{liquid}: 1.72 (21 %)	30		
					Cp_{liquid}: 1.80 (28 %)	60		
	SiO_2	0.5	Aqueous solution + sonication + drying in hot plate	SEM, DLS, TGA, DSC	Cp_{liquid}: 1.53±0.09 (3.41%)	12	The mechanism involved in the specific heat increment was proven to be based on a surface phenomenon	[89]
		1			Cp_{liquid}: 1.85±0.06 (25.03%)			
		1.5			Cp_{liquid}: 1.51±0.09 (2%)			
		2			Cp_{liquid}: 1.53±0.12 (3.69%)			
	Al_2O_3	0.9 (vol.%)	Aqueous solution + sonication + drying in hot plate	SEM, EDS, Optical Microscope, DSC	Cp results are shown in figures. Cp are all between 1.35 and 1.6, less than the solar salt results	13	The reduction of the specific heat of nanofluid when nanoparticles size reduces was found to be due to the nanolayer effect	[90]
		2.7 (vol.%)						
		4.6 (vol.%)						
		0.9 (vol.%)				90		
		2.7 (vol.%)						
		4.6 (vol.%)						
	CuO	0.1		XRD, DSC	Cp_{solid}: (4.55%)	10–20		[91]

			Grinded + mixing + heating + grinded		Cp_{liquid}: (6.86%)		The mixing model with an intermediate layer can be used to predict specific heat enhancement at low particle concentrations	
		0.5			Cp_{solid}: (7.96%) Cp_{liquid}: (11.48%)			
		1.0			Cp_{solid}: (-1.14%) Cp_{liquid}: (-1.27%)			
		2.0			Cp_{solid}: (-1.67%) Cp_{liquid}: (-0.19%)			
		3.0			Cp_{solid}: (-1.22%) Cp_{liquid}: (-0.15%)			
	CuO	2 % vol.	Not specified	FTIR, SEM, LFA, DSC/TGA	$k_{solid} < 0.6$	40	Other thermophysical properties are also measured and also for pure salts (KNO_3 and $NaNO_3$)	[84]
Hitec Salt (NaNO3 (7% mol.) + KNO3 (53% mol.) + NaNO2 (40% mol.))	Al_2O_3	0.016	Mixing + melting + stirring	SEM, DSC	Cp_{liquid}: 1.49±0.02 (9.6%)	<50	The agglomeration becomes significant and the particle clusters seem to be inter-connected at high concentrations	[92]
		0.063			Cp_{liquid}: 1.63±0.03 (19.9%)			
		0.125			Cp_{liquid}: 1.53±0.02 (12.7%)			
		0.25			Cp_{liquid}: 1.49±0.02 (9.6%)			
		0.5			Cp_{liquid}: 1.46±0.02 (7.8%)			
		1			Cp_{liquid}: 1.45±0.02 (6.5%)			
		2			Cp_{liquid}: 1.32±0.02 (-2.7%)			
Ternary nitrate salt (67%KNO3, 19% Ca(NO3)2·4H2O and 14% LiNO3)	CuO	0.5	Aqueous solution + sonication + drying in a rotary evaporator	SEM, transient plane source technique, TGA/DSC	Cp_{liquid}: 2.125 k_{liquid}: 0.5200	200	It is observed that sedimentation of nanoparticles in molten salt is negligible compared to that in organic heat transfer fluids	[93]
		1			Cp_{liquid}: 0.5–1.0 k_{liquid}: 0.5210			
		2			Cp_{liquid}: ~1.0 k_{liquid}: 0.5010			
	MoS_2	0.5			Cp_{liquid}: 2.385 k_{liquid}: 0.5211			
		1			Cp_{liquid}: 0.5–0.75 k_{liquid}: 0.5312			
		2			Cp_{liquid}: 0.75-1.0 k_{liquid}: 0.5011			
Binary carbonate salt Li_2CO_3- K_2CO_3, 62:38 molar ratio)	SiO_2	1	Aqueous solution + sonication + drying in a hot plate	SEM, DSC	Cp_{liquid}: 1.97±0.05 (24%)	5	The observed enhancement in Cp can be explained by the high specific surface energies that are associated with the high surface areas of the embedded nanoparticles and the needle-like structures	[94]
					Cp_{liquid}: 2.01±0.07 (26%)	10		
					Cp_{liquid}: 1.95±0.07 (23%)	30		
					Cp_{liquid}: 2.00±0.03 (26%)	60		

Ternary carbonate salt K_2CO_3-Li_2CO_3-Na_2CO_3 (4:4:2, mass ratio)	SiO_2	1	Aqueous solution + sonication + drying in an electric thermostatic drying oven	SEM, XRD,TGA/DSC	Cp_{liquid}: 3.49±0.08 (116.8%)	5	The dispersive state of nanoparticles and the resulting amount of needle-like nanostructures in ternary carbonates nanofluids bring about the difference in the enhanced specific heat capacity	[95]
					Cp_{liquid}: 3.44±0.08 (113.7%)	20		
					Cp_{liquid}: 3.28±0.04 (103.7%)	30		
					Cp_{liquid}: 2.74±0.23 (70.2%)	60		
Chloride salt $BaCl_2$ (34%) + NaCl (13%) + $CaCl_2$ (40%) + LiCl (13%)	SiO_2	1	Aqueous solution + sonication + drying in a hot plate	SEM, DSC	Cp_{liquid}: 0.98±0.03 (14.5%)	20-30	Three independent thermal transport mechanisms are proposed to explain the enhancement of Cp	[96]

76

3.2.1. Nanoparticles added to nitrates

Chieruzzi et al. [82] synthesized nanofluids based on solar salt with three different nanoparticles—SiO_2, Al_2O_3, and a mix of SiO_2/Al_2O_3—with 1 wt.% concentration using a twin-screw microcompounder, varying the speed and time. The authors characterized the nanofluids in terms of heat of fusion and specific heat by DSC. From the results, it can be concluded that heat of fusion is not remarkably increased (less than 7.5%) and the specific heat is sometimes increased, depending on the nanoparticle and the synthesis procedure. The best results are obtained with the nanofluid produced with SiO_2/Al_2O_3 nanoparticles at 200 rpm for 30 min, giving a Cp that is 18.5% (1.936 J/g·ºC) higher when compared to the solar salt (1.632 J/g·ºC). The same authors did a previous study with the two-steps methodology, finding that the highest increase in Cp (22.5%) was for 1 wt.% of SiO_2/Al_2O_3 [96]. They also state that adding nanoparticles to the base salt increased the heat of fusion of the nanofluid compared to the base salt (with 1 wt.%).

An enhancement of around 28% of the specific heat of the solar salt (1.47±0.02 J/g·ºC) was achieved by Dudda and Shin [89] when adding 1 wt.% of 60-nm SiO_2 nanoparticles. Smaller particle sizes (5, 10, and 30 nm) were also tested. Similar results were obtained by Andreu-Cabedo et al. [89], with an increment of 25% of Cp when working with 12-nm SiO_2 nanoparticles and 1 wt.% concentration. In the case of mixing solar salt with Al_2O_3 nanoparticles, Lu and Huang [90] observed no enhancement in Cp in the liquid phase. Luo et al. [92] studied the Cp of the solar salt when adding CuO nanoparticles, finding that the maximum enhancement of specific heat occurred at a nanoparticle concentration of 0.5 wt.%—with 7.96% increment for the solid phase and 11.48% increment for the liquid phase.

Myers et al. [83] investigated the effect on thermal conductivity enhancement due to adding CuO nanoparticles to KNO_3, $NaNO_3$, and the solar salt composition. Thermal conductivity of the solid phase of these nanofluids is calculated (see Eq. 9) from the experimental diffusivity and properties obtained from the literature. Solar salt shows the highest improvement with 2 vol.% CuO.

Ho and Pan [92] investigated the effect of adding nanoparticles, at seven different concentrations, of alumina in Hitec salt, $NaNO_3$ (7%) + KNO_3 (53%) + $NaNO_2$ (40%).

An optimal concentration of 0.063 wt.% was identified as yielding the greatest enhancement of specific heat capacity of 19.9% at 275ºC.

Madathil et al [93] presents results of a ternary salt, 67%KNO_3, 19% $Ca(NO_3)_2 \cdot 4H_2O$, and 14% $LiNO_3$, with MoS_2 and CuO, separately, at three different concentrations. Phase-change temperature and enthalpy, thermal stability, specific heat capacity, and thermal conductivity were evaluated. The major achievements were in thermal conductivity. The authors concluded that no general trend exists in the results and the exact mechanism of thermal conductivity characteristics of nanofluids is not well understood. From the results, one can conclude that the highest thermal conductivity corresponds to samples containing 0.5% and 1% nanoparticle concentration.

3.2.2. Nanoparticles added to carbonates

Tiznobaik and Shin [94] found that the specific heat capacity of the nanofluid based on a binary carbonate salt, Li_2CO_3-K_2CO_3, 62:38 molar ratio, with SiO_2 was enhanced by 25%, regardless of the size of the nanoparticles.

Sang and Liu [95] synthesized several ternary carbonate nanofluids of K_2CO_3-Li_2CO_3-Na_2CO_3 (4:4:2, mass ratio) with nanoparticles by using the two-steps solution method. They investigated the specific heat capacity of ternary carbonates nanofluids with four different nanoparticles (SiO_2, CuO, TiO_2, Al_2O_3) and SiO_2 with different sizes (5, 20, 30, 60 nm). The results for SiO_2-based nanofluid are shown in Table 5 because these nanoparticles were the most effective additive among of the four tested nanoparticles in enhancing the specific heat capacity of ternary carbonates. A maximum enhancement of 116.8% was achieved with 5-nm SiO_2 at 540ºC in the specific heat capacity of ternary carbonates.

3.2.3. Nanoparticles added to chlorides

Shin and Banerjee [96] synthesised and characterized a eutectic chloride salt, $BaCl_2$ (34%) + NaCl (13%) + $CaCl_2$ (40%) + LiCl (13%), with 1% of SiO_2 nanoparticles concentration. The specific heat capacity was enhanced by 14.5%.

This topic is gaining attention and the publications related are increasing exponentially. This technology is still at a very low technology readiness level (TRL); therefore, several steps and more research are needed to overcome the present barriers. Despite presenting some differences in ultrasonic bath time and in evaporation method and temperature, the Shin and Banerjee methodology [96] is being followed currently to produce molten-salt nanofluids. However, other methodologies are being developed because the methodology needs to be viable for scale-up.

In general terms and from the published results presented in Table 5, molten salts present greater enhancement opportunities of Cp than of thermal conductivity. Specific methods to test thermophysical properties need to be developed to have comparable and reproducible results. Less dispersion in the results is required to ensure the potential of these nanofluids for industrial applications.

Moreover, molecular dynamics is crucial for modelling these fluids and for a deeper understanding of the theory behind it and for the basics of the phenomena that can explain at the molecular level the enhancement of some thermophysical properties. Other tests required to implement this breakthrough technology at large-scale applications need to evaluate its thermal performance and the stability under dynamic conditions and real operating conditions (temperature and pressure).

In addition, any enhancements in thermal properties (specific heat capacity or thermal conductivity) should be qualified by considering the associated changes in the rheological properties (e.g., increase in viscosity). The operational efficiencies for a particular application (e.g., CSP/TES, thermal management) depend on the operation strategy and level of enhancement in the rheological properties. For example, in power tower configurations of the CSP stations, the effect of viscosity enhancement is likely to be marginal compared to that of parabolic trough configurations in CSP plants [91]. The cost-benefit analysis for mixing Hitec-Solar Salt with nanoparticles was studied by Malik [87] using the "Excelergy Model" developed at the National Renewable Energy Laboratory (NREL). The analyses showed that if the cost of adding nanoparticles into Hitec increases the material cost by ~10%, and if this causes specific heat capacity enhancement of 20%, then the cost of power generated by a CSP plant can be reduced by ~10% [88].

4. Next-generation CSP plants

4.1. High-temperature molten salts

To achieve high thermal-to-electric conversion efficiency and to lower electricity production from renewables, different initiatives have been launched from Europe (FP7 and H2020 programs) and the USA (SunShot Initiative). These initiatives focus on next-generation CSP increasing the cost competitiveness with conventional electric power generation. Higher efficiencies could be obtained by integrating a CSP plant with a supercritical CO_2 (s-CO_2) Brayton power cycle. To achieve this integration, CSP needs to operate at temperatures above 550°C, which requires high-temperature advanced fluids in the range of 550°C to 750°C; see Figure 20.

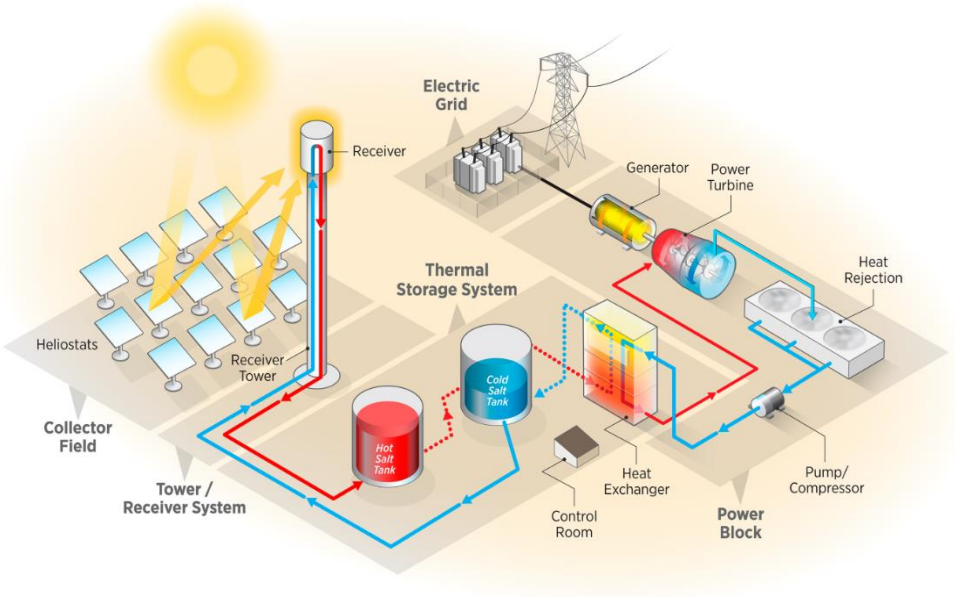

Figure 20. Gen3 CSP molten-salt power tower with direct storage using higher salt temperatures to integrate with a s-CO_2-Brayton power cycle [98].

Based on the thermal carrier physical state in the solar receiver, CSP stakeholders defined three potential pathways: molten salt, particle, or gaseous. Because there is no change from current state-of-the-art power tower design, molten-salt systems represent the most familiar approach; however, significant material challenges will be faced because of the increase in the maximum operating temperature from 565°C to about 720°C. New salts are required to operate in this higher temperature range because nitrates are unstable at temperatures above 600°C. The selection of a high-temperature molten-salt chemistry is

needed, as well as considering its impact on containment materials that can achieve acceptable strength, durability, and cost targets at these high temperatures [99]. Possible candidates are chloride and carbonate salt blends, but each brings new challenges associated with thermal properties, costs, and corrosion. CSP component designers required reliable and accurate data with the new salt chemistry selected and corrosion mechanisms need to be very well established. The state-of-the-art commercial nitrate salts, currently used in CSP plants, are unstable at temperatures above 620°C [13]. It has been proposed to use a high-oxygen-content ullage gas to increase this temperature limit by stabilizing the nitrate anion. But it is understood that nitrates will not reach temperatures necessary to achieve the power-cycle efficiency goals, i.e., ≥ 700°C [100].

Favourable thermophysical properties and chemical characteristics for heat transfer and energy storage are low melting point, high heat capacity, high thermal conductivity, thermal stability up to about 750°C, chemical compatibility with CO_2, and low corrosion behaviour with cost-effective containment materials [99]. The ternary eutectic carbonate $Na_2CO_3/K_2CO_3/Li_2CO_3$ has excellent energy density, higher than nitrate solar salt, because it has a higher heat capacity (~1.6 J/g·K) and a larger liquid density (~2 kg/L) [105]. If this eutectic carbonate is used as the HTF/TES, the storage tanks could be reduced in size compared with a state-of-the-art TES system using nitrates. It has been reported that this eutectic carbonate is stable up to around 800°C in inert atmospheres [101]. If a CO_2 blanket is used, the onset of decomposition is extended to above 1,000°C, with weight loss due to salt evaporation starting at 788°C. Under air, the carbonate system is less stable, having a decomposition starting at 601°C with a rapid rate of weight loss at 673°C [102]. The main disadvantage that makes this eutectic carbonate unable to be used in CSP plants is the cost. The battery market drives the cost of Li, which makes this blend extremely expensive for the CSP industry.

Because of their low cost and high decomposition temperatures, molten chlorides are being considered as good candidates. However, these molten salts introduce a set of technological and engineering challenges because of their very corrosive characteristics for typical materials. Corrosion mitigation approaches have been investigated to obtain degradation of containment materials of around 20 μm/yr or lower; thus, they provide a lifetime for CSP plants of 30 years or more [103–109].

Significant data exist regarding state-of-the-art nitrate solar salt corrosion performance with alloys up to about 620°C as well as its thermophysical properties (heat capacity, density, viscosity, and thermal conductivity). Based on the limited literature with reliable, consistent, and accurate high-temperature salt mixtures adequate for CSP applications, three chloride salt chemistries have been used as possible candidates. Table 6 reports important physical properties of the candidates' high-temperature salts compared with baseline nitrate solar salt. Volume change on melting was also reported because it is an important criterion for freeze recovery. Additional validation R&D testing is required to down-select the blend that will offer the best opportunity for success.

Table 6. Candidate molten-salt heat-transfer fluids and approximate physical properties, or for the pure components if mixture data are not available [98].

Salt	**Mass fraction**	**Melting point (°C)**	**Heat capacity (J/g-K)**	**Density (kg/L)**	**Δ Volume on melting**	**Notes****	**Ref.**
$NaNO_3$ KNO_3 (baseline)	0.60 0.40	220	1.52	1.7	+4.6%	-	[47,81,109]
$ZnCl_2$ NaCl KCl	0.686 0.075 0.239	204	0.81	2.4	NaCl/KCl: +14.8% NaCl: +26.1% KCl: +22.3% [14]	ZnCl BP(732°C) [15]	[47]
$MgCl_2$ KCl	0.375 0.625	426	1.15	1.66	KCl: +22.3% $MgCl_2$: +30.5% [14]	$MgCl_2$ BP(1412°C)	[110]
$MgCl_2$ KCl NaCl	~0.34 – 0.68 ~0.18 – 0.51 ~0.14 – 0.25	~380°C – 396°C	1.05–1.15	–	NaCl: +26.1% KCl: +22.3% $MgCl_2$: +30.5% [14]		[110]

**BP(XXX°C): boiling-point temperature.

Over the last several decades, physical property data have been recorded for solar salt over the range of its normal operating conditions of 300°C to 600°C [109]. A similar level of knowledge is required for the salts listed in Table 6 because accurate physical property data are important to design piping, solar receiver, and heat exchangers.

Due to their low cost and high decomposition temperatures, molten chlorides are the top candidates. However, these molten salts introduce a set of technological and engineering

challenges because of their very corrosive characteristics for typical materials. Corrosion in molten chlorides is controlled in atmospheres without oxygen and water. If these impurities are present, molten chlorides become very corrosive in the liquid and vapour phases. Catastrophic mechanical failure is then possible because intergranular attack is the corrosion mode [47,110].

The typical corrosion mode under aerobic conditions is pitting and intergranular. Most chromia-forming alloys exhibit localized corrosion in the presence of oxygen [103,104,111]. Alloys form oxides that eventually dissolve into the molten chloride salt, liberating the oxygen component that then later is able to maintain the oxidization process. Intergranular corrosion is the major type of corrosion in these alloys exposed to molten chlorides in oxidizing atmosphere.

Chromia-forming alloys, Fe-based and Ni-based, do not show corrosion resistance in molten chlorides. It has been reported that increasing Cr content in those alloys produced an increase in corrosion rates whereas changes in nickel content showed no effect [112]. The mechanism was associated with the higher solubility of Cr_2O_3 in molten chlorides compared with those of iron and nickel oxides [113,114].

Corrosion of nickel-based alloys was found to increase with increasing partial pressure of oxygen [115] and water vapours [116]. The effect of water vapour and oxygen in the cover gas of CSP systems must be evaluated, monitored, and controlled.

NaCl–LiCl

NREL evaluated the behavior of AISI stainless steels 310 (SS310), 347 (SS347), Incoloy 800H (In800H), and Inconel 625 (IN625) in eutectic 34.42 wt.% NaCl – 65.58 wt.% LiCl at 650°C and 700°C in nitrogen atmosphere [102]. Electrochemical evaluations using open-circuit potential (OCP) followed by potentiodynamic polarization sweep (PPS) or linear-sweep voltammetry (LSV) were employed. A three-electrode arrangement was used with a Pt-wire pseudo reference electrode (RE), a Pt-mesh counter electrode (CE), and the working electrode (WE) being sampled. The data were analysed using Tafel slopes and the Faraday law to determine the corrosion rates.

The alloys showed active corrosion under an imposed anodic potential. The alloy SS347 with the lower nickel content of only 9.62 wt.% reported the highest corrosion rate of 7.49±0.32 mm/year. It was reported that higher nickel concentration is required for corrosion-resistance behaviour against molten chloride systems. The nickel superalloy IN625 with Ni > 58 wt.% and low amount of iron (< 5 wt.% Fe) was the most corrosion-resistant alloy against molten NaCl–LiCl at 650°C, with a corrosion rate of 2.80±0.38 mm/year. The high corrosion rates observed were probably associated with the initial condition of the molten salts. These tests were performed with salts in as-received condition without further purification. It was reported that a temperature increase of only 50°C more than doubled the corrosion rate of SS 310 and In800H compared to the initial 650°C test.

Inductively coupled plasma–mass spectrometry (ICP-MS) analysis of the salts after corrosion showed that, in general, the amount of Cr, Mn, and Fe dissolved into the molten salt at 650°C and 700°C increased in the following order: IN625 < In800H < SS310. These results corroborate the corrosion rates obtained from the electrochemical tests in which the susceptibility to corrosion of the alloys increased in the same order. When the corrosion temperature increased from 650°C to 700°C, more Cr, Mn, and Fe dissolved from the alloys into the molten salt.

In800H performed slightly better than SS310; however, top-view metallographic analysis with a field emission-scanning electron microscope (FESEM) resolved localized (intergranular or pitting) corrosion. The corroded surface of IN625 showed some extent of localized corrosion, but lower than in SS310 and In800H. It was reported that Cr and Fe were preferentially corroded from SS310, In800H, and IN625 because EDX analyses reported depletion of chromium and iron near the corroded surfaces. SS310 produced Cr oxide and mixed oxides enriched in Ni with small amounts of Fe and Cr. For In800H, the presence of Ni-Cr-Fe-Mn-Ti was observed and IN625 showed the presence of Cr-Fe oxide. Different oxide morphologies were resolved. Granular oxide morphology consisted of Ni oxide with small amounts of Cr and Fe resolved as well as a needle-type morphology identified as Cr oxide. These results indicate that oxygen contamination of the salts could have caused a large amount of corrosion. In the presence of oxygen-containing compounds, the alloy forms oxides that eventually dissolve into the molten

chloride salt, liberating the oxygen component that later is able to maintain the oxidization process.

For CSP applications, corrosion rates of a few millimetres per year cannot be sustained. Corrosion rates of molten-salt containment alloys should be lower than 20 µm/year. Additionally, localized corrosion is very common in chloride systems, and the failure of alloys through this corrosion mode can be catastrophic. Thus, corrosion-mitigation approaches are required so that advanced CSP plants can meet cost-reduction targets. It has been reported that in an oxygen-free system, fewer corrosion products would be transported, fewer cathodic reactions will be in place (oxidizer effect), and thus, less corrosion will occur.

NaCl–KCl

Liu et al. [117] performed isothermal corrosion of TP347H, C22 alloys, and laser-cladding C22 coatings in molten 98.6 wt.% KCl - 1.4 wt.% NaCl at 450°–750°C. They reported two corrosion mechanisms as a function of temperature: chemical corrosion dominating at lower temperature and electrochemical corrosion control at higher temperatures. At lower temperatures, accelerated oxidation by Cl^- and Cl species occurs, often referred to as active oxidation.

Electrochemical corrosion mode dominating at higher temperatures increased because of the dissolution of protective surface oxide scale by the molten chloride salts. Accelerated corrosion occurs because of the presence of aggressive impurities, such as oxygen, with the ability to reach the alloy surface and diffuse in the alloy substrate.

NaCl-$MgCl_2$

Corrosion mechanisms of pure nickel (Ni), GH4033, and GH4169 at 793 K in molten eutectic NaCl-$MgCl_2$ were studied by Wang et al. [118]. Corrosion resistance of pure Ni was better than GH4033 and GH4169, where Cr and Fe preferentially oxidized to later be chlorinated.

$ZnCl_2$-based molten salts

Vignarooban et al. [119] studied the corrosion resistance of Hastelloys C-276, C-22, and N types in molten eutectics containing NaCl, KCl, and $ZnCl_2$ and determined that Hastelloys N reported corrosion rates higher than C-276 and C-22, even though Hastelloy N has higher nickel content. The higher corrosion was associated with the lower Cr content (7%) in Hastelloy N compared to C-276 and C-22. This is contrary to many other reported results, which implies the need to study the synergistic effects of alloying elements on the corrosion resistance of the alloys in molten chlorides.

$MgCl_2$–KCl using Mg to control corrosion

Corrosion in molten salts can be controlled using electrochemical approaches. Some researchers proposed the redox potential control using active metals such as Mg to reduce corrosion rates to below 10 µm/year at 800°C; but the use of no oxygen or water in the atmosphere is also required [120–121].

Ding et al. [122] have performed cyclic voltammetry to identify the corrosive hydroxide impurities present in the ternary salt composed by $MgCl_2$/KCl/NaCl (60/20/20 mol%). This mixture was also evaluated by Ding et al. [123] at 700ºC, performing corrosion tests on three commercial alloys (SS310, Incoloy 800H, Hastelloy C-276) during 500 hours, but the requirements for commercial applications (corrosion rate <10 microns/year) could not be obtained.

Surface modifications as control corrosion

Vapour pressures of chlorides are high enough that, in combination with oxygen, gaseous compounds will produce a harsh atmosphere that is generally very aggressive to common chromia-forming alloys. Corrosion mitigations must consider a solution in which both zones (immersed in fluid and exposed to vapour phase) will be protected. The active-metal approach can protect the alloys under immersion conditions, but the areas exposed to chloride vapours will not be protected. To address this, corrosion mitigation approaches have been proposed using surface treatments such as *in-situ* passivation, pre-oxidation, coatings, and diffusive coatings such as boronizing and aluminizing. Surface modification

may be an interesting approach because the alloy could then be exposed to both the liquid and the vapour phases of the salt mixture even if chemistry change.

4.3. Materials and components at high storage temperature

Higher-temperature CSP system components require materials and designs that are amenable to both transients (e.g., cold and overnight start-up, clouds, wind) and long-life operation. Designs must satisfy both mechanical and chemical compatibility in high-temperature environments that range from 540ºC to 750ºC [99]. This does not require projects to invent entirely new sets of practices [75] because previous designs and components can be applied to new projects. However, it is important to determine the specific requirements based on overall system operation that significantly differ from current CSP technologies and that will require adjustment.

Higher-temperature components have significant thermal-mechanical requirements that include cold start-up thermal cycles, diurnal thermal cycling, and rates of thermal change consistent with CSP plant operation. Requirements differ on a component-by-component basis, depending on functionality. For example, the receiver may have a daily requirement of cold start (20ºC) to operational temperature (700ºC–750ºC); over a 30-year plant life, this corresponds to roughly 11,000 thermal cycles. Heat exchangers, by contrast, may circulate molten salt at night and may only require two cold starts per year, corresponding to less than 100 cold-start thermal cycles over a 30-year operational lifetime. Each system, subsystem, and component (e.g., piping systems, salt storage tanks, valves, pumps, heat exchangers, salt instrumentation, heat tracing) requires an independent analysis. Once specific requirements are provided for components, equipment must then be designed and fabricated to meet the required design standards.

No CSP standards currently exist, so much of the design work will be driven from sections of the ASME Boiler and Pressure Vessel Code (BVPC), ASME piping standards, and American Petroleum Institute (API) standards. For example, the nitrate salt receiver at Solar Two was designed per Power Boiler (i.e., Section I) of the BPVC and Code Case N-47. Power boilers typically operate at high pressures (>950 psi) and are subjected to strain within elastic limit. Although the Solar Two receiver was held at pressures below 400 psi, the strain imposed was above the elastic regime and required use of N-47. N-47

informed the receiver design, avoiding creep failure modes (rupture and fatigue). In addition, piping must be designed using various piping standards, such as ASME B31.1 and ASME B31.3. All of the standards mentioned here help guide the design of robust thermal-mechanical systems, but none of the standards provide directive guidance on corrosion and chemical compatibility.

To guide materials selection for chemical compatibility and corrosion, industry should leverage a series of compatibility tests with both materials in the current codes, and new materials that show promise for CSP demanding requirements. Chemical compatibility with halide salts requires either selection of a thermodynamically stable material or a diffusion barrier to prevent corrosion. Thermodynamic stability can be assessed by minimizing the potential for chemical reaction between the containment material and salt by choosing containment materials that have more positive Gibbs free energy of formation relative to the salt (i.e., less likely to form metal chloride). Chlorides of alkali metals and alkali-earth elements (i.e., KCl, NaCl, LiCl, $MgCl_2$) are very stable, whereas containment metals are less stable as chlorides (i.e., $NiCl_2$, $CrCl_2$, $MoCl_5$, $FeCl_2$). In comparing molybdenum vs. chromium, using the information in Figure 21, metallic molybdenum should be more effective in preventing corrosion than metallic chromium because chromium would be more susceptible to oxidization and subsequent formation of $CrCl_2$, which is soluble in the melt. Materials that behave as diffusion barriers may react readily with the environment; an example of this is the use of chromium in high-temperature steam systems. Alloys with chromium are preferred because chromium is readily oxidized to thin, protective chrome oxide. This oxide prevents diffusion of oxygen into the base material and self-heals due to the chromium content in the alloy. Chromium is soluble in molten-salt systems and cannot be used; however, finding parallels in chlorides might be the selection of materials that form insoluble, adherent chlorides, where one example is $TaCl_5$ [103]. To date, molten-chloride systems for CSP have used thermodynamically stable alloys, where high nickel content with minimum chromium improves performance [108,124,125], and this approach is well documented for nuclear power applications.

One example of a thermodynamically stable alloy is Hastelloy N (also called INOR-8) used during the Molten Salt Reactor Experiment (MSRE) [125], which was selected to contain a LiF-BeF_2-U_xF_y. Hastelloy N is a nickel-based alloy that replaced chromium

with molybdenum to minimize the formation of CrF_2, which is soluble in the melt. Selection of alloys, or relatively noble, pure metals (e.g., nickel or molybdenum), with low chromium content ensures better corrosion performance. Use of ceramics has been limited in molten-salt systems for power applications, but surface treatments could also include compatible ceramic materials to prevent corrosion. No oxides can be used in fluoride systems, but based on high-temperature oxidation of NiCrAl thermal spray [125], it appears that oxides may be viable protective coatings; however, they would require thorough experimental testing before industrial application.

Compatible materials, such as Hastelloy N or ceramic liners, are not yet qualified for mechanical use in the BPVC or various piping codes required for designs. Therefore, use of these materials for chemical compatibility require their application as a liner or clad. Liners can be applied via surface treatments, such as physical deposition or chemical vapour deposition, whereas cladding can be added by a variety of techniques, such as cold rolling or welding. Liners and clad are recognized by both the B31.1 and B31.3 piping codes as allowable techniques for protecting pipes from corrosion and erosion. Readers are referred to paragraph 124.8 in ASME B31.1-2014 [126] and paragraph 323.4.3 in ASME B31.3-2012 [127] for specific usages of liners and clad.

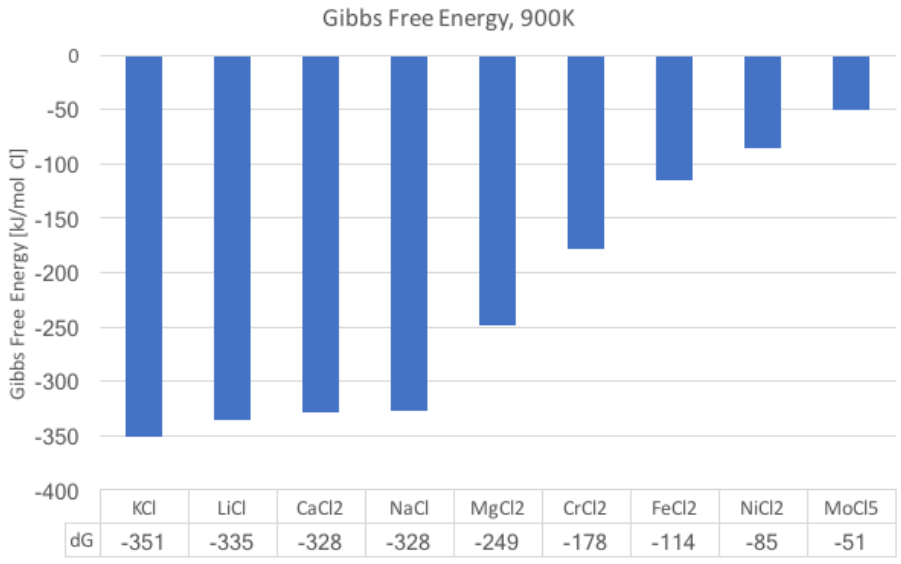

Figure 21. Gibbs free energy (per Cl basis) of metal chlorides [128].

5. Conclusions

Today's most-advanced CSP systems are towers using molten salts as TES material. At the moment, current prices (0.165 €/kWh) indicate that CSP plants are more mature and the cost of electricity production is competitive compared with other renewable and fossil fuel sources, but additional improvements can be made.

We have done a comprehensive review of the current status of molten salts used in commercial projects as well as the new trends for improving TES systems. Regarding the current TES systems:

- Addition of new alkali or alkali-earth nitrate components have been analysed using $LiNO_3$, $Ca(NO_3)_2$, $NaNO_2$, $CsNO_3$, and $Mg(NO_3)_2$. According to the thermophysical properties obtained, $LiNO_3$ is the best candidate to be added to the solar salt to increase the work temperature range in CSP plants. However, the high cost of this additive is an important drawback for their development.
- Addition of different nanoparticles (SiO_2 and Al_2O_3) to solar salts. Doping molten salts with 1 wt.% of nanoparticles increases the heat capacity (20% higher in some cases) and also appears to enhance thermal conductivity.

Finally, we discussed the need for a different molten-salt chemistry to achieve higher thermal-to-electric conversion, and the use of carbonate and/or chloride molten salts appears as the most feasible option. However, these molten salts introduce a set of technological and engineering challenges:

- High corrosion behaviour in conventional materials.
- Corrosion mitigation strategies need to be addresses for successfully developing this new generation of CSP plants.
- Chloride salt blends showed that impurities—in particular, oxygen and moisture—significantly exacerbate corrosion.
- The use of these chlorides as HTF/TES requires chemical purification and pre-melting procedures under vacuum or dry/inert atmospheres with chemically controlled addition of other compounds/elements. The nature and concentration of impurities in the salt must be identified to define the acceptable composition

and its levels. If physi- and chemisorbed water is not removed and salt purification is not performed prior to melting, then the salt will react to form undesired secondary phases—such as HCl and hydroxychlorides—that can promote corrosion.

- A unique chloride composition must be selected to further evaluations such as corrosion and chemical compatibility, and thus, to determine the containment materials for each CSP system and component. The efficient design of these components depends greatly on materials for fabrication and thermal transfer.
- Salt handling, melting, purification, and ullage gas protocols, design, and operation of critical subsystems (TES, system sizing, receiver, heat trace, valves, pumps, and primary heat exchanger) depend greatly on the HTF/TES chemistry.

Acknowledgements

The research leading to these results has received funding from the Spanish government (ENE2015-64117-C5-1-R (MINECO/FEDER)). The authors thank the Catalan Government for the quality accreditation given to their research group GREiA (2017 SGR 1537). GREiA is a certified agent TECNIO in the category of technology developers from the Government of Catalonia. Angel G. Fernández acknowledges the financial support provided by CONICYT/FONDAP 15110019 “Solar Energy Research Center” SERC-Chile. Dr. Aran Solé thanks Ministerio de Economía y Competitividad de España for Grant Juan de la Cierva, FJCI-2015-25741. Dr. Eduard Oró thanks Ministerio de Economia y Competitividad de España for Grant Juan de la Cierva IJCI-2016-30568.

This work was authored in part by the National Renewable Energy Laboratory, operated by Alliance for Sustainable Energy, LLC, for the U.S. Department of Energy (DOE) under Contract No. DE-AC36-08GO28308. Funding provided by U.S. Department of Energy, Office of Energy Efficiency and Renewable Energy, Solar Energy Technologies Office, Concentrating Solar Power. The views expressed in the article do not necessarily represent the views of the DOE or the U.S. Government. The U.S. Government retains and the publisher, by accepting the article for publication, acknowledges that the U.S. Government retains a nonexclusive, paid-up, irrevocable, worldwide license to publish or reproduce the published form of this work, or allow others to do so, for U.S. Government purposes.

551

552 **References**

553

554 [1] REN21, 2017. Renewables 2017 Global Status Report, Paris.

555 [2] National Renewable Energy Laboratory (NREL). Project listing. Available online:
556 https://www.nrel.gov/csp/solarpaces/ (Accessed November 2017).

557 [3] CSP World website. Available online: http://cspworld.org/cspworldmap (Accessed
558 November 2017).

559 [4] A. Gil, M. Medrano, I. Martorell, A. Lázaro, P. Dolado, B. Zalba, L.F. Cabeza. State of
560 the art on high temperature thermal energy storage for power generation. Part 1—
561 Concepts, materials and modellization. Renewable and Sustainable Energy Reviews 14
562 (2010) 31–55.

563 [5] P. Gauché, J. Rudman, M. Mabaso, W.A.Landman, T.W. von Backström, A.C. Brent.
564 System value and progress of CSP. Solar Energy 152 (2017) 106–139.

565 [6] M.J. Vasallo, J.M. Bravo, E.G. Cojocaru, M.E. Gegúndez. Calculating the profits of an
566 economic MPC applied to CSP plants with thermal energy system. Solar Energy 155
567 (2017) 1165–1177.

568 [7] IRENA (2017), Electricity storage and renewables: Costs and markets to 2030,
569 International Renewable Energy Agency, Abu Dhabi.

570 [8] W. González-Roubaud, D. Pérez-Osorio, C. Prieto. Review of commercial thermal energy
571 storage in concentrated solar power plants: Steam vs. molten salts. Renewable and
572 Sustainable Energy Reviews 90 (2017) 133–148.

573 [9] U. Pelay, L. Luo, Y. Fan, D. Stitou, M. Rood. Thermal Energy storage systems for
574 concentrated solar power plants. Renewable and Sustainable Energy Reviews 79 (2017)
575 82–100.

576 [10] Technology Roadmap. Solar Thermal Electricity. International Energy Agency, 2014.

577 [11] G. M. Kaplan, Understanding solar concentrators, Arlington, VA: Volunteers in Technical
578 Assistance, 1985.

579 [12] Sandia National Laboratories, Final Test and Evaluation Results from the Solar Two
580 Project, Sandia National Laboratories, Albuquerque, 2002.

581 [13] R. Bradshaw and S. Goods, Accelerated Corrosion Testing of a Nickel-Base Alloy in a
582 Molten Salt, SAND2001-8758, Sandia National Laboratories, Albuquerque, 2001.

583 [14] B. Kelly, Lessons Learned, Project History, and Operating Experience of the Solar Two
584 Project, Sandia National Laboratories, Albuquerque, 2000.

585 [15] R. Bradshaw, S. Goods, Corrosion of Alloys and Metals by Molten Nitrates, Sandia
586 National Laboratories, Albuquerque, 2001.

587 [16] D. Nissen, D. Meeker, Nitrate/nitrite chemistry in sodium nitrate-potassium nitrate melts,
588 Inorganic Chemistry, 22(5) (1983) 716–721.
589 [17] J. Cordaro, Chemical perspectives on alkali and earth alkaline nitrate and nitrite salts for
590 concentrated solar power applications, Green 3(1) (2013).
591 [18] R. Bradshaw, N. Siegel, Molten nitrate salt development for thermal energy storage in
592 parabolic trough solar power systems, ES2008-54174, in Energy Sustainability 2008,
593 Jacksonville, 2008.
594 [19] FactSage, FTsalt - FACT Salt Phase Diagrams,
595 http://www.crct.polymtl.ca/fact/documentation/FTsalt/FTsalt_Figs.htm, 2017.
596 [20] G. Smith, Corrosion of Materials in Fused Hydroxides, ORNL-2048, Oak Ridge National
597 Laboratory, Oak Ridge, 1958.
598 [21] R. Rapp, J. Devan, D. Douglass, P. Nordine, F. Pettit, D. Whittle, High temperature
599 corrosion in energy systems, Materials Science and Engineering 50(1) (1981) 1–17.
600 [22] R. Koripelli, D. Crowe, D. French, J. Brand, The Role of Fireside Corrosion on Boiler
601 Tube Failures, Part I, Power, 01 04 (2010).
602 [23] I. Singh, U. Sen, Influence of temperature and sulphate ion on corrosion of mild steel in
603 molten $NaNO_3$, British Corrosion Journal 27(4) (1992).
604 24. C. Prieto, C. Rubio Abujas, F.J. Ruiz-Cabañas, A. Rodríguez-Sanchez, A.I. Fernández,
605 M. Martínez, E. Oró, L.F. Cabeza. Effect of the impurity magnesium nitrate in the thermal
606 decomposition of the Solar Salt. Submitted to Solar Energy (2018).
607 [25] National Renewable Energy Laboratory, Concentrating Solar Power Projects with
608 Operational Plants, 24 11 2017. [Online]. Available:
609 https://www.nrel.gov/csp/solarpaces/projects_by_status.cfm?status=Operational.
610 [26] R. Devaradjane. Utilization of molten nitrate salt nanomaterials for heat capacity
611 enhancement in solar power applications. University of Texas at Arlington, 2013.
612 [27] ASTM E1269 – 11. Standard Test Method for Determining Specific Heat Capacity by
613 Differential Scanning Calorimetry
614 [28] G. Ferrer, C. Barreneche, A. Solé, I. Martorell, L. F. Cabeza, New proposed methodology
615 for specific heat capacity determination of materials for thermal energy storage (TES) by
616 DSC. Journal of Energy Storage 11 (2017) 1–6.
617 [29] B. Muñoz-Sánchez. A precise method to measure the specific heat of solar salt-based
618 nanofluids. Journal of Thermal Analysis Calorimetry 129 (2017) 905–914.
619 [30] http://www.tainstruments.com/pdf/literature/TN34.pdf (last accessed 28/11/2017)
620 [31] B. Muñoz-Sánchez, J. Nieto-Maestre, J. Gonzalez-Aguilar, J.E. Juliá, N. Navarrete, A.
621 Faik, T. Bauer, A. Bonk, M.E. Navarro, Y. Ding, N. Uranga, E. Veca, S. Sau, P.
622 Giménez, P. Garcia, J.I. Burgaleta. Round Robin Test on the Measurement of the Specific

623 Heat of Solar Salt. International Conference on Concentrating Solar Power and Chemical
624 Energy Systems, SolarPACES 2016, 11.-14.10.2016, Abu Dhabi, United Arab Emirates.
625 [32] S. Gschwander, T. Haussmann, G. Hagelstein, A. Sole, G. Diarce, W. Hohenauer, D.
626 Lager, C. Rathgeber, P. Hennemann, A. Lazaro, H. Mehling. Standard to Determine the
627 Heat Storage Capacity of PCM using hf-DSC with Constant Heating/Cooling Rate
628 (Dynamic Mode). DSC 4229 PCM Standard. A technical report of subtask A2.1 of IEA-
629 SHC 42 / ECES Annex 29 (2015).
630 [33] A. Solé, L. Miró, C. Barreneche, I. Martorell, L.F. Cabeza. Review of the T-history
631 method to determine thermophysical properties of phase change materials (PCM),
632 Renewable and Sustainable Energy Reviews 26 (2013) 425–436.
633 [34] J.W. Raade, D. Padowitz. Development of molten salt heat transfer fluid with low melting
634 point and high thermal stability. ASME J Sol Energy Eng 133 (2011) 031013.
635 [35] T. Bauer, N. Pfleger, N. Breidenbach, M. Eck, D. Laing, S. Kaesche. Material aspects of
636 Solar Salt for sensible heat storage. Applied Energy 111 (2013) 1114–1119.
637 [36] G. Ferrer, A. Solé, C. Barreneche, I. Martorell, L.F. Cabeza. Review on the methodology
638 used in thermal stability characterization of phase change materials. Renewable and
639 Sustainable Energy Reviews 50 (2015) 665–685.
640 [37] M.V. Smirnov, V.A. Khokhlov, E.S. Filatov. Thermal conductivity of molten alkali
641 halides and their mixtures. Electrochimica Acta 32(7) (1987) 1019–1026.
642 [38] An, X.H., Cheng, J.H., Yin, L.D., Xie, L.D., Zhang, P. Thermal conductivity of high
643 temperature fluoride molten salt determined by laser flash technique. International Journal
644 of Heat and Mass Transfer 90 (2015) 872–877.
645 [39] K.M. Pramod, P.V.C. Rao, N.V. Choudary, K. Ramesh. Novel methodology to prepare
646 homogenous ternary molten salts for concentrated solar power applications and their
647 thermo-physical characterization. Applied Thermal Engineering 109 (2016) 906–910.
648 [40] Q. Peng, J. Ding, X. Wei, J. Yang, X. Yang. The preparation and properties of multi-
649 component molten salts. Applied Energy 87 (2010) 2812–2817.
650 [41] R.H. Perry, D.W. Green, eds. (1997). Perry's Chemical Engineers' Handbook (7th ed.).
651 McGraw-Hill. ISBN 0-07-049841-5
652 [42] R.B. Cundall, T.F. Palmer, C.E.C. Wood. Vapour pressure measurements on some
653 organic high explosives. Journal of the Chemical Society, Faraday Transactions 1:
654 Physical Chemistry in Condensed Phases 74 (1978) 1339–1345.
655 [43] Y. Rong, C.M. Gregson, A. Parker. Thermogravimetric measurements of liquid vapor
656 pressure. The Journal of Chemical Thermodynamics 51 (2012) 25–30.
657 [44] A. Meffre, N. Tessier-Doyen, X. Py, M. Huger, N. Calvet. Thermomechanical
658 characterization of waste based TESM and assessment of their resistance to thermal
659 cycling up to 1000°C. Waste Biomass Valor 7 (2016) 9–21.

[45] IEA (2010). Concentrating Solar Power Roadmap. http://www.iea.org/publications/freepublications/publication/csp_roadmap.pdf.

[46] M. Liu, N. H. Steven Tay, S. Bell, M. Belusko, R. Jacob, G. Will, W. Saman, F. Bruno. Review on concentrating solar power plants and new developments in high temperature thermal energy storage technologies. Renewable and Sustainable Energy Reviews 53 (2016) 1411–1432.

[47] K. Vignarooban, X. Xu, A. Arvay, A.M. Kannan. Heat transfer fluids for concentrating solar power systems—A review. Applied Energy 146 (2016) 383–396.

[48] W. Michel (1993). Heat transfer fluid of potassium nitrate lithium nitrate and 0 to 38% calcium nitrate. US5244592.

[49] R.W. Bradshaw. (2010). Viscosity of Multicomponent Molten Nitrate Salt-Liquidus to 200ºC. Sandia report.

[50] Y. Jin, J. Cheng, et al. Accurate viscosity measurement of nitrates/nitrites salts for concentrated solar power. Solar Energy 137 (2016) 385–392.

[51] R. Kniep. (1997). Salt mixtures for storing thermal energy in the form of heat of phase transformation. US5591374.

[52] N. Lotz. (2003). Salt mixtures for storing thermal energy in the form of heat of phase transformation. US6627106.

[53] J.W. Raade, D. P. (2010). Development of molten salt heat transfer fluid with low melting point and high thermal stability. SolarPACES Conference.

[54] J.W. Raade, D. P., J. Vaughn (2011). Low melting point molten salt heat transfer fluid with reduced cost. SolarPACES Conference.

[55] A.G. Fernandez, H. Galleguillos, E. Fuentealba, F. Perez, Thermal characterization of Hitec molten salt for energy storage in solar linear concentrated technology. Journal of Thermal Analysis and Calorimetry 122 (2015) 3–9.

[56] R.I. Olivares. The thermal stability of molten nitrite/nitrates salt for solar thermal energy storage in different atmospheres. Solar Energy 86(9) (2012) 2576–2583.

[57] N. Boerema, G. Morrison, Liquid sodium versus Hitec as a heat transfer fluid in solar thermal central receiver systems. Solar Energy 86(9) (2012) 2293–2305.

[58] A.G. Fernandez, S. Ushak, H. Galleguillos, F. Perez. (2014). Development of new molten salts with $LiNO_3$ and $Ca(NO_3)_2$ for energy storage in CSP plants. Applied Energy 119 (2014) 131–140.

[59] A.G. Fernandez, J. Vidal-Gomez. (2016). Thermophysical properties of low cost lithium nitrate salts produced in northern Chile for thermal energy storage. Renewable Energy 101 (2017) 120–125.

[60] R.W. Bradshaw, D.E. Meeker. High-temperature stability of ternary nitrate molten salts for solar thermal energy systems." Solar Energy Materials 21(1) (1990) 51–60.

[61] J.C Gomez, N. Calvet, A. Starace, G. Glatzmaier, $Ca(NO_3)_2$-$NaNO_3$-KNO_3 molten salt mixtures for direct thermal energy storage systems in parabolic trough plants. Journal of Solar Energy Engineering 135(2) (2013) 021016–021016.

[62] C. Parrado, A. Marzo, E. Fuentealba, A.G. Fernandez. 2050 LCOE improvement using new molten salts for thermal energy storage in CSP plants. Renewable and Sustainable Energy Reviews 57 (2016) 505–514.

[63] E.M. Levin, Phase diagram for ceramist. American Ceramic Society 1 (1964).

[64] F. Xu, J. Wang, Thermodynamic modeling and experimental verification of a $NaNO_3$-KNO_3-$LiNO_3$-$Ca(NO_3)_2$ system for solar thermal energy storage. New Journal of Chemistry 41(18) (2017) 10376–10382.

[65] J. Wang, M. Lai, Thermodynamic modeling and experimental verification of eutectic point in the $LiNO_3$-KNO_3-$Ca(NO_3)_2$ ternary system. Journal of Thermal Analysis and Calorimetry 119(2) (2015) 1259–1266.

[66] R.I. Olivares, W. Edwards. $LiNO_3$-$NaNO_3$-KNO_3 salt for thermal energy storage: Thermal stability evaluation in different atmospheres. Thermochimica Acta 560(0) (2013) 34–42.

[67] T. Wang, D. Mantha, R. Reddy, Thermodynamic properties of $LiNO_3$-$NaNO_3$-KNO_3-$2KNO_3{\cdot}Mg(NO_3)_2$ system. Thermochimica Acta 551(0) (2013) 92–98.

[68] T. Wang, D. Mantha, R. Reddy, Novel low melting point quaternary eutectic system for solar thermal energy storage. Applied Energy 102(0) (2013) 1422–1429.

[69] N. Ren, Y.-T. Wu, C.-F. Ma, L.-X. Sang, Preparation and thermal properties of quaternary mixed nitrate with low melting point. Solar Energy Materials and Solar Cells 127 (2014) 6–13.

[70] M.B. Mehedi, G. A. Brooks, Thermal analysis of molten ternary lithium-sodium-potassium nitrates. Renewable Energy 104 (2017) 76–87.

[71] A.G. Fernandez, S. Ushak, H. Galleguillos, F. Perez, Thermal characterisation of an innovative quaternary molten nitrate mixture for energy storage in CSP plants. Solar Energy Materials and Solar Cells 132 (2014) 172–177.

[72] S. Sau, N. Corsaro, et al. Techno-economic comparison between CSP plants presenting two different heat transfer fluids. Applied Energy 168 (2016) 96–109.

[73] G.J. Janz, G.N Truong. Melting and premelting properties of the KNO_3-$NaNO_2$-$NaNO_3$ eutectic system. J Chemistry Engineering 28 (1983) 201–202.

[74] D.A. Nissen. Thermophysical properties of the equimolar mixture $NaNO_3$-KNO_3 from 300 to 600°C. J Chem Eng Data 27(3) (1982) 269–273.

[75] A.B. Zavoico. Solar power tower design basis document. SAND 2001

[76] T. Bauer, D. L., R. Tamme. Recent progress in alkali nitrate/nitrite developments for solar thermal power applications. Molten Salt Chemistry and Technology Conference (2011).

[77] W. Brockner, M. Gjikaj. Thermal decomposition of nickel nitrate hexahydrate, $Ni(NO_3)_2 \cdot 6H_2O$, in comparison to $Co(NO_3)2 \cdot 6H_2O$ and $Ca(NO_3)2 \cdot 4H_2O$. Thermochimica Acta 456(1) (2007) 64–68.

[78] J. Paulik, M. Arnold. Thermogravimetric examination of the dehydration of calcium nitrate tetrahydrate under quasi-isothermal and quasi-isobaric conditions. Journal of Thermal Analysis 27 (1983) 409–418.

[79] Y. Grosu, O. Bondarchuk, A. Faik, The effect of humidity, impurities and initial state on the corrosion of carbon and stainless steels in molten HitecXL salt for CSP application. Solar Energy Materials and Solar Cells 174 (2018) 34–41.

[80] A.G. Fernandez, F. J. Perez. Improvement of the corrosion properties in ternary molten nitrate salts for direct energy storage in CSP plants. Solar Energy 134 (2016) 468–478.

[81] A.G. Fernandez, S. Veliz, H. Galleguillos, Thermal characterization of solar salts from north of Chile and variations of their properties over time at high temperature. Journal of Thermal Analysis and Calorimetry 128(3) (2017) 1241–1249.

[82] M. Chieruzzi, G.F. Cerritelli, A. Miliozzi, J.M. Kenny, L. Torre. Heat capacity of nanofluids for solar energy storage produced by dispersing oxide nanoparticles in nitrate salt mixture directly at high temperature. Solar Energy Materials and Solar Cells 167 (2017) 60–69.

[83] P.D. Myers, Jr., T.E. Alam, R. Kamal, D.Y. Goswami, E. Stefanakos. Nitrate salts doped with CuO nanoparticles for thermal energy storage with improved heat transfer. Applied Energy 165 (2016) 225–233.

[84] H. Riazi, T. Murphy, G. Webber, R. Atkin, S. S. M. Tehrani, R. A. Taylor. Specific heat control of nanofluids: A critical review. International Journal of Thermal Sciences 107 (2016) 25–38.

[85] J. Buongiorno. Conventional transport in nanofluids, ASME J. Heat Transfer 128 (2006) 240–250.

[86] R. Hentschke. On the specific heat capacity enhancement in nanofluids. Nanoscale Research Letters 11 (2016) 88.

[87] D.R. Malik. Evaluation of Composite Alumina Nanoparticle and Nitrate Eutectic Materials for Use in Concentrating Solar Power Plants, MS Thesis, Texas A&M University, College Station, TX, USA (2010).

[88] B. Dudda, D. Shin. Effect of nanoparticle dispersion on specific heat capacity of a binary nitrate salt eutectic for concentrated solar power applications. International Journal of Thermal Sciences 69 (2013) 37–42.

[89] P. Andreu-Cabedo, R. Mondragon, L. Hernandez, R. Martinez-Cuenca, L. Cabedo, J. E. Julia. Increment of specific heat capacity of solar salt with SiO_2 nanoparticles. Nanoscale Research Letters 9 (2014) 582.

[90] M.C. Lu, C.H. Huang. Specific heat capacity of molten salt-based alumina nanofluids. Nanoscale Research Letters 8 (2013) 292–299.

[91] Y. Luo, X. Du, A. Awad, D. Wen. Thermal energy storage enhancement of binary molten salt via in-situ produced nanoparticles, International Journal of Heat and Mass Transfer 104 (2017) 658–664.

[92] M. Ho, C. Pan. Optimal concentration of alumina nanoparticles in molten Hitec salt to maximize its specific heat capacity, International Journal of Heat and Mass Transfer 70 (2017) 174–184.

[93] P.K. Madathil et al., Preparation and characterization of molten salt based nanothermic fluids with enhanced thermal properties for solar thermal applications. Applied Thermal Engineering 109 (2016) 901–905.

[94] H. Tiznobaik, D. Shin. Enhanced specific heat capacity of high-temperature molten salt-based nanofluids. International Journal of Heat and Mass Transfer 57 (2013) 542–548.

[95] L. Sang, T. Liu. The enhanced specific heat capacity if ternary carbonates nanofluids with different nanoparticles. Solar Energy Materials and Solar Cells 169 (2017) 297–303.

[96] D. Shin, D. Banerjee. Enhancement of specific heat capacity of high-temperature silica-nanofluids synthesized in alkali chloride salt eutectics for solar thermal-energy storage applications. International Journal of Heat and Mass Transfer 54 (2011) 1064–1070.

[97] M. Chieruzzi, G.F. Cerritelli, A. Miliozzi, J.M. Kenny. Effect of nanoparticles on heat capacity of nanofluids based on molten salts as PCM for thermal energy storage. Nanoscale Research Letters 8 (2013) 448.

[98] M. Mehos, C. Turchi, J. Vidal, M. Wagner, Z. Ma, C. Ho, W. Kolb, C. Andraka, A. Kruizenga. Concentrating Solar Power Gen3 Demonstration Roadmap. Technical Report NREL/TP-5500-67464. January 2017.

[99] M. Kruizenga, W. Kolb, R. J. Briggs, J. Christian, D. Ray, D. Gill, J. Kelton, K. Chisman, Loop for the Observation of Film Temperature Effects on Decomposition (LOFTED), Sandia Report SAND2014-18103, September 2014.

[100] X. An et al., Determination and evaluation of the thermophysical properties of an alkali carbonate eutectic molten salt, Faraday Discuss. 190 (2016) 327.

[101] R. I. Olivares, C. Chen, S. Wright, The thermal stability of molten lithium–sodium–potassium carbonate and the influence of additives on the melting point, Journal of Solar Energy Engineering 134 (2012) 041002-1–8.

[102] J.C. Gomez-Vidal, R. Tirawat. Corrosion of alloys in a chloride molten salt (NaCl–LiCl) for solar thermal technologies. Sol. Energ. Mat. Sol. C 157 (2016) 234–244.

[103] J.C. Gomez-Vidal, A.G. Fernandez, R. Tirawat, C. Turchi, W. Huddleston. Corrosion resistance of alumina forming alloys against molten chlorides for energy production. I:

806 pre-oxidation treatment and isothermal corrosion tests. Sol. Energ. Mat. Sol. C 166,
807 (2017) 222–233.
808 [104] J.C. Gomez-Vidal, A.G. Fernandez, R. Tirawat, C. Turchi, W. Huddleston. Corrosion
809 resistance of alumina forming alloys against molten chlorides for energy production. II:
810 Electrochemical impedance spectroscopy under thermal cycling conditions. Sol. Energ.
811 Mat. Sol. C 166 (2017) 234–245.
812 [105] K. Vignarooban, P. Pugazhendhi, C. Tucker, D. Gervasio, A.M. Kannan. Corrosion
813 resistance of Hastelloys in molten metal-chloride heat-transfer fluids for concentrating
814 solar power applications. Sol. Energy 103 (2014) 62–69.
815 [106] A.M. Kruizenga. Corrosion mechanisms in chloride and carbonate salts. Sandia Report
816 SAND2012-7594 (2012).
817 [107] J.C. Gomez-Vidal, J. Noel, J. Weber. Corrosion evaluation of alloys and MCrAlX
818 coatings in molten carbonates for thermal solar applications. Sol. Energ. Mat. Sol. C 157,
819 (2016) 517–525.
820 [108] J.C. Gomez-Vidal, E. Morton. Castable cements to prevent corrosion of metals in molten
821 salts. Sol. Energ. Mat. Sol. C 153 (2016) 44–51.
822 [109] SQM, SQM's Thermo-Solar Salts (Salt Factsheet), Antwerpen, Belgium: SQM Europe,
823 N.V. (www.sqm.com) (2016).
824 [110] Williams, Assessment of Candidate Molten Salt Coolants for the NGNP/NHI Heat-
825 Transfer Loop, ORNL/TM-2006/69, Oak Ridge, TN (2006).
826 [111] B. Liu, X. Wei, W. Wang, J. Lu, J. Ding. Corrosion behavior of Ni-based alloys in molten
827 NaCl-$CaCl_2$-$MgCl_2$ eutectic salt for concentrating solar power. Solar Energy Materials
828 and Solar Cells 170 (2017) 77–86.
829 [112] M.S. Sohal, M.A. Ebner, P. Sabhar, Engineering database of liquid salt thermophysical,
830 Technical Report (2010).
831 [113] Y.S. Li, M. Spiegel, S. Shimada, Corrosion behaviour of various model alloys with NaCl-
832 KCl coating, Mater. Chem. Phys. 93 (2005) 217–223.
833 [114] T. Ishitsuka, K. Nose, Stability of protective oxide films in waste incineration
834 environment – solubility measurement of oxides in molten chlorides, Corros. Sci. 44
835 (2002) 247–263.
836 [115] A. Rahmel, Corrosion, in: D.G. Lovering (Ed.), Molten Salt Technology, Plenum Press,
837 New York, (1982) 265–283.
838 [116] P.D. Myers, D.Y. Goswami, Thermal energy storage using chloride salts and their
839 eutectics, Appl. Therm. Eng. 109 (2016) 889–900.

[117] S.N. Liu, Z.D. Liu, Y.T. Wang, J. Tang, A comparative study on the high temperature corrosion of TP347H stainless steel, C22 alloy and laser-cladding C22 coating in molten chloride salts, Corros. Sci. 83 (2014) 396–408.

[118] J.W. Wang, C.Z. Zhang, Z.H. Li, H.X. Zhou, J.X. He, J.C. Yu, Corrosion behavior of nickel-based superalloys in thermal storage medium of molten eutectic NaCl- $MgCl_2$ in atmosphere, Sol. Energy Mater. Sol. Cells 164 (2017) 146–155.

[119] K. Vignarooban, P. Pugazhendhi, C. Tucker, D. Gervasio, A.M. Kannan, Corrosion resistance of Hastelloys in molten metal-chloride heat-transfer fluids for concentrating solar power applications, Sol. Energy 103 (2014) 62–69.

[120] B. A. T. Mehrabadi, J. W. Weidner, B. Garcia-Diaz, M. Martinez-Rodriguez, L. Olson, S. Shimpalee, Multidimensional modeling of nickel alloy corrosion inside high temperature molten salt systems. Journal of The Electrochemical Society 163 (2016) 830–838.

[121] B. A. T. Mehrabadi, J. W. Weidner, B. Garcia-Diaz, M. Martinez-Rodriguez, L. Olson, S. Shimpalee, Modeling the effect of cathodic protection on superalloys inside high temperature molten salt systems. Journal of The Electrochemical Society 164 (2017) 171–179.

[122] W. Ding, A. Bonk, J. Gussone, T. Bauer. Electrochemical measurement of corrosive impurities in molten chlorides for thermal energy storage. Journal of Energy Storage 15 (2018) 408–414.

[123] W. Ding, H. Shi, Y. Xiu, A. Bonk, A. Weisenburger, A. Jianu, T. Bauer. Hot corrosion behavior of commercial alloys in thermal energy storage material of molten $MgCl_2$/KCl/NaCl under inert atmosphere. Solar Energy Materials and Solar Cells 184 (2018) 22–30.

[124] H.-S. Cho, J. Van Zee, S. Shimpalee, B. Tavakoli, J. Weidner, B. Garcia-Diaz, M. Martinez-Rodriguez, L. Olson, J. Gray, Dimensionless Analysis for Predicting Fe-Ni-Cr Alloy Corrosion in Molten Salt Systems for Concentrated Solar Power Systems, Corrosion 72(6) (2016) 742–760.

[125] J. Lane, Fluid fuel reactors, Addison-Wesley Pub. Co. (1958).

[126] American Society of Mechanical Engineers, Power Piping: ASME Code for Pressure Piping, B31.1, ASME, New York (2014).

[127] American Society of Mechanical Engineers, Process piping: ASME Code for Pressure Piping, B31.3, ASME, New York (2012).

[128] C. Ho, B. Iverson, Review of high-temperature central receiver designs for concentrating solar power, Renewable and Sustainable Energy Reviews 29 (2014) 835–846.

Annex 1. Information on commercial CSP plants

Name of the project	Status	Country	Technology	Capacity [MW]	Annual electricity generation [MWh]	HTF	TES	Storage type	TES capacity [hours]	Cost		PPA	
Abhijeet Solar Project	U Cons.	India	PTC	50	N.A.	Thermal oil	No			N.A.		12.24	Rs per kWh
Agua Prieta II	U Cons.	Mexico	PTC	12	34,000	Thermal oil	No			N.A.		N.A.	
Alba Nova I	U Cons.	France	LFR	12	414,000	Water/Steam	Yes	Saturated Steam	1	N.A.		N.A.	
Al Abdaliyah Integrated Solar Combined Cycle	U Dev.	Kuwait	PTC	60	N.A.	N.A.	N.A.			N.A.		N.A.	
Ashlim	U Dev.	Israel	PTC	110	N.A.	N.A.	Yes	Molten salts 2-tank indirect	4.5	1	b.US$	0.76	NIS per kWh
Ashlim Plot B (Megalim)	U Cons.	Israel	Tower	121	N.A.	Water/Steam	No			N.A.		0.79	NIS per kWh
Atacama-1	U Cons.	Chile	Tower	110	N.A.	Molten salts	Yes	Molten salts 2-tank direct	17.5	N.A.		N.A.	
Aurora Solar Energy Project	U Dev.	Australia	Tower	150	N.A.	Molten salts	Yes	Molten salts 2-tank direct	8	650	m.AU$	N.A.	
Bokpoort	U Cons.	South Africa	PTC	50	230,000	Thermal oil	Yes	Molten salts 2-tank indirect	9.3	300	m.€	N.A.	
Centrale Solaire Thermoynamique Llo	U Dev.	France	LFR	9	N.A.	HTF: water	Yes	Saturated Steam	1	N.A.		N.A.	
Chabei 64 MW Molten Salt Parabolic Through project	U Dev.	China	PTC	64	N.A.	Molten salts	Yes	Molten salts 2-tank direct	16	N.A.		N.A.	
Copiapó	U Dev.	Chile	Tower	260	1,800,000	N.A.	Yes	Molten salts 2-tank direct	14	N.A.		N.A.	
Dacheng Dunhuang 50 MW Molten Salt Fresnel project	U Dev.	China	LFR	50	N.A.	N.A.	Yes	Molten salts 2-tank direct	13	N.A.		N.A.	
Dadri ISCC Plant	U Cons.	India	LFR	14	14,000	Water/Steam	No			N.A.		N.A.	
Delingha 50 MW Thermal oil Parabolic Trough project	U Cons.	China	PTC	50	N.A.	Thermal oil	Yes	Molten salts 2-tank indirect	9	N.A.		N.A.	
Diwakar	U Cons.	India	PTC	100	N.A.	Thermal oil	Yes	Molten salts 2-tank indirect	4	N.A.		10.5	Rs per kWh
eLLO Solar Thermal Project (Llo)	U Cons.	France	LFR	9	20,200	Water/Steam	Yes	Saturated Steam	4	N.A.		N.A.	
Gansu Akesai 50 MW Molten Salt Trough project	U Dev.	China	PTC	50	N.A.	N.A.	Yes	Molten salts 2-tank direct	15	N.A.		N.A.	
Golden Tower 100 MW Molten Salt project	U Dev.	China	Tower	100	N.A.	N.A.	Yes	Molten salts 2-tank direct	8	N.A.		N.A.	
Golmund	U Cons.	China	Tower	200	1,120,000	Molten salts	Yes	Molten salts 2-tank direct	15	5380	m.RMB	N.A. N.A.	

Gujarat	U Cons.	India	PTC	20	N.A.	N.A.	N.A.			N.A.		N.A.	
Gujarat Solar One	U Cons.	India	PTC	25	130,000	Thermal oil	yes	Molten salts 2-tank indirect	9	N.A.		N.A.	
Gulang 100 MW Thermal Oil Parabolic Trough project	U Dev.	China	PTC	100	N.A.	N.A.	Yes	Molten salts 2-tank indirect	7	N.A.		N.A.	
Hami 50 MW CSP Project	U Dev.	China	Tower	50	N.A.	Molten salts	Yes	Molten salts 2-tank direct	8	N.A.		N.A.	
Huanghe Qinghai Delingha 135 MW DSG Tower CSP Project	U Dev.	China	Tower	135	628,448	Water/Steam	Yes	Molten salts 2-tank indirect	3.7	N.A.		1.15	Yuan/kWh
HelioFocus China Orion Project	U Cons.	China	Parabolic Dish	60	N.A.	Air	N.A.			N.A.		N.A.	
Helios Power	U Dev.	Cyprus	Parabolic Dish	50.76	N.A.	N.A.	N.A.			N.A.		N.A.	
Hidden Hills SEGS	U Dev.	US	Tower	500	N.A.	N.A.	N.A.			N.A.		N.A.	
Ilanga I	U Dev.	South Africa	PTC	100	N.A.	Thermal oil	Yes	Molten salts 2-tank indirect	4.5	N.A.		N.A.	
ISCC Duba 1	U Cons.	Saudi Arabia	PTC	43	N.A.	Thermal oil	No			N.A.		N.A.	
Kathu Solar Park	U Cons.	South Africa	PTC	100	N.A.	Thermal oil	yes	Molten salts 2-tank indirect	4.5	N.A.		N.A.	
Kaxu Solar One	U Cons.	South Africa	PTC	100	N.A.	Thermal oil	Yes	Molten salts 2-tank indirect	2.5	860	m.US$	0.32	$ per kWh
Khi Solar One	U Cons.	South Africa	Tower	50	N.A.	Water/Steam	Yes	Saturated Steam	3	450	m.US$	N.A.	
Kogan Creek Solar Boost (Kogan Creek)	U Cons.	Australia	LFR	44	44,000	Water/Steam	No			105	m.AU$	N.A.	
Kom Ombo CSP project	U Dev.	Egypt	PTC	100	N.A.	N.A.	N.A.			N.A.		N.A.	
KVK Energy Solar Project	U Cons.	India	PTC	100	N.A.	Thermal oil	Yes	Molten salts 2-tank indirect	4	N.A.		11.2	Rs per kWh
Maximus Dish Project	U Dev.	Greece	Parabolic Dish	75	N.A.	N.A.	N.A.			N.A.		N.A.	
Mazara Solar	U Dev.	Italy	Tower	50	N.A.	Water/Steam	Yes	Saturated Steam		N.A.		N.A.	
Megha Engineering	U Cons.	India	PTC	50	N.A.	N.A.	Yes	Molten salts 2-tank indirect	8	140	m.US$	11.31	INR per kWh
MINOS	U Dev.	Greece	Tower	52	N.A.	N.A.	Yes	Molten salts 2-tank indirect	5	N.A.		0.278	€/kWh
Ningxia ISCC	U Cons.	China	PTC	92	N.A.	N.A.	N.A.			2300	m.CNY	N.A.	
NOOR II	U Cons.	Morocco	PTC	185	N.A.	Thermal oil	Yes	Molten salts 2-tank indirect	7	N.A.		1.36	MAD per kWh
NOOR III	U Cons.	Morocco	Tower	135	N.A.	Molten salts	Yes	Molten salts 2-tank direct	7	N.A.		1.42	MAD per kWh
Ouarzazate	U Cons.	Morocco	PTC	160	N.A.	N.A.	Yes	Molten salts 2-tank indirect	3	1042	m.€	1.62	MAD per kWh
Ouarzazate 2	U Dev.	Morocco	Tower	100	N.A.	N.A.	Yes	N.A.		N.A.		N.A.	
Ouarzazate 3	U Dev.	Morocco	PTC	200	N.A.	N.A.	Yes	N.A.		N.A.		N.A.	

Palen SEGS	U Dev.	US	Tower	500	N.A.	Water/Steam	No			N.A.		N.A.	
Planta Solar Cerro Dominador (Atacama 1)	U Cons.	Chile	Tower	110	N.A.	Molten salts	Yes	Molten salts 2-tank direct	24	1.3	b.US$	N.A.	
Planta Solar Cerro Dominador (Atacama 2)	U Cons.	Chile	Tower	110	N.A.	N.A.	Yes	Molten salts 2-tank direct	24	N.A.		N.A.	
Planta Termosolar Pedro de Valdivia	V Dev.	Chile	PTC	360	N.A.	N.A.	N.A.			2610	m.US$	N.A.	
Qinghai Gonghe 50 MW CSP Plant	U Dev.	China	Tower	50	N.A.	Molten salts	Yes	Molten salts 2-tank direct	6	N.A.		N.A.	
Rayspower Yumen 50 MW Thermal Oil Trough project	U Cons.	China	PTC	50	N.A.	Thermal oil	Yes	Molten salts 2-tank indirect	7	N.A.		1.15	RMB/kWh
Redstone Solar Thermal Power Plant	U Dev.	South Africa	Tower	100	480,000	Molten salts	Yes	Molten salts 2-tank direct	12	N.A.		0.124	$/kWh
Rice Solar Energy Project	U Dev.	US	Tower	150	488,000	Molten salts	Yes	Molten salts 2-tank direct	10	600	m.US$	N.A.	
Shagaya CSP Project	U Dev.	Kuwait	PTC	50	N.A.	N.A.	Yes	Molten salts 2-tank indirect	10	N.A.		N.A.	
Shangyi 50 MW DSG Tower CSP project	U Dev.	China	Tower	50	N.A.	Water/Steam	Yes	Molten salts 2-tank indirect	4	N.A.		N.A.	
SunCan Dunhuang 100 MW Phase II	U Cons.	China	Tower	100	N.A.	Molten salts	Yes	Molten salts 2-tank direct	11	N.A.		N.A.	
Sundt Solar Boost	U Dev.	US	LFR	5	N.A.	N.A.	N.A.			N.A.		N.A.	
Supcon Solar Project	U Cons.	China	Tower	50	120,000	Molten salts	Yes	Molten salts 2-tank direct	6	750	m.RMB	N.A.	
TuNur	U Dev.	Tunisia	Tower	2000	N.A.	N.A.	N.A.			N.A.		N.A.	
Urat 50 MW Fresnel CSP project	U Dev.	China	LFR	50	N.A.	Thermal oil	Yes	Molten salts 2-tank indirect	6	N.A.		N.A.	
Urat Middle Banner 100 MW Thermal Oil Parabolic Trough project	U Cons.	China	PTC	100	N.A.	Thermal oil	Yes	Molten salts 2-tank indirect	4	N.A.		N.A.	
Waad Al Shamal ISCC Plant	U Cons.	Saudi Arabia	PTC	50	N.A.	Thermal oil	No			N.A.		N.A.	
Xina Solar One	U Dev.	South Africa	PTC	100	N.A.	N.A.	Yes	Molten salts 2-tank indirect	5	N.A.		N.A.	
Yumen 100 MW Molten Salt Tower CSP project	U Dev.	China	Tower	100	N.A.	Molten salts	Yes	Molten salts 2-tank direct	10	N.A.		N.A.	
Yumen 50 MW Molten Salt Tower CSP project	U Cons.	China	Tower	50	N.A.	Molten salts	Yes	Molten salts 2-tank direct	9	1790	m.CNY	N.A.	
Yumen 50 MW Mthermal Oil Trough CSP project	U Dev.	China	PTC	50	N.A.	Thermal oil	Yes	Molten salts 2-tank indirect	7	N.A.		N.A.	
Zhangbei 50 MW CSG Fresnel CSP project	U Dev.	China	LFR	50	N.A.	Water/Steam	Yes	Concrete	14	N.A.		N.A.	
Zhangjiakou 50 MW CSG Fresnel project	U Dev.	China	LFR	50	N.A.	Water/Steam	Yes	Concrete	14	N.A.		N.A.	

878 **Annex 2. International currency equivalence to the Euro**

879

International currency equivalence to Euro			
1	US$	0.850	€
1	RMB	0.128	€
1	AU$	0.666	€
1	CNY	0.128	€
1	Rs	0.013	€
1	NIS	0.242	€
1	MAD	0.090	€

880